Frequency Design of Three-phase Active Front-End Converter with Reduced Filter in EV Chargers

Wu, Yang; Xu, Junzhong; Soeiro, Thiago Batista; Bauer, Pavol; Qin, Zian

DOI
10.1109/TTE.2024.3381167

Publication date
2024

Document Version
Final published version

Published in
IEEE Transactions on Transportation Electrification

Frequency Design of Three-Phase Active Front-End Converter With Reduced Filter in EV Chargers

Yang Wu, *Student Member, IEEE*, Junzhong Xu, *Member, IEEE*, Thiago Batista Soeiro, *Senior Member, IEEE*, Pavol Bauer, *Senior Member, IEEE*, and Zian Qin, *Senior Member, IEEE*

***Abstract*— In recent years, significant research and adoption of periodic variable-switching frequency pulsewidth modulation (PWM) (P-VSFPWM) have been observed in ac/dc voltage source converters (VSCs). This technique aims to reduce ripple in ac inductor current and dc capacitor voltage, suppress injected current harmonic amplitudes for electromagnetic compatibility (EMC) compliance, and minimize switching losses. However, the presence of overlapped harmonic spectra from different switching harmonic bands can lead to heightened harmonic magnitudes due to the wide-frequency variation, necessitating additional filtering measures. Surprisingly, there is notable absence of harmonic spectra analysis under P-VSFPWM, despite the growing concern over supraharmonics (2–150 kHz) emission injected to the grid from the electric-vehicle (EV) chargers. To address this gap, this article proposes the interleaved P-VSFPWM to mitigate harmonics overlap without deviating from the intended purpose of P-VSFPWM. A fast-acquisition supraharmonics model under arbitrary P-VSFPWM has been proposed based on vectorization, facilitating the subsequent filter design process. Furthermore, this study identifies the optimal P-VSFPWM profile with minimal required filtering inductance based on the spectra analysis. These findings are verified by PLECS simulations and experimental results.**

***Index Terms*— Filter reduction, harmonics model, periodic variable-switching frequency pulsewidth modulation (PWM) (P-VSFPWM).**

I. Introduction

ENHANCING power and gravimetric density holds significant importance for the application of electric-vehicle (EV) battery chargers [1], [2], [3], [4], [5]. Pulsewidth-modulation (PWM)-based voltage source converters (VSCs) are preferably employed as the active front-end (AFE) ac/dc converters in the two-stage EV chargers illustrated in Fig. 1 because of their robustness and simplicity [6]. Compared with constant switching frequency PWM (CSFPWM), variable-switching frequency PWM (VSFPWM) is commonly utilized in the AFE converter of onboard EV chargers to achieve higher power density. It has been particularly used in ac/dc PWM-based VSCs for diverse applications and purposes, such as switching loss minimization [7], [8], [9], [10], zero-voltage switching (ZVS) [11], [12], [13], [14], ripple reduction of the converter, such as the inductor current and dc-link capacitor voltage [15], [16], [17], [18], and improvement of the conducted electromagnetic interference (EMI) [19], [20], [21], [22], [23], [24], [25], [26].

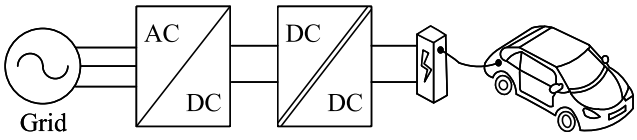

Fig. 1. Diagram of a typical two-stage three-phase EV charger.

Table I summarizes the information of the implemented VSFPWM methods from the aforementioned studied literature works. Among all the VSFPWM methods, the periodicity was exhibited in the variable-switching frequency profile. It is important to note that frequency profiles predominantly cluster within the supraharmonics range (2–150 kHz). In recent studies, supraharmonics have been reported to significant impact on low-voltage distribution grids during the EV charging process because of the high switching frequency for PWM [27], [28], [29]. This range has gained significant attention from the international standard-setting community due to recent efforts to restrict emissions. EV chargers can potentially introduce supraharmonic distortions into the power grid, as switching frequencies within this range are frequently employed to achieve efficient and cost-effective power converter designs. This is especially pronounced in the case of onboard chargers, where considerations, such as weight and size, further drive the adoption of switching frequencies within the supraharmonic range [29], [30]. More importantly, these periodic VSFPWM (P-VSFPWM) methods also feature a widespread spectrum caused by the wide-frequency variation setting Δf_c. The spectrum width of each carrier-frequency harmonic band can be estimated by Carson's rule [23]. Therein, the parameter $\delta = \Delta f_c / f_{c0}$ has been used to quantify the overlap between

Manuscript received 9 November 2023; revised 11 February 2024; accepted 16 March 2024. Date of publication 25 March 2024; date of current version 27 December 2024. This work was supported in part by the European H2020 Research and Innovation Program (Power2Power Project), Electronic Components and Systems for European Leadership (ECSEL) Joint Undertaking; and in part by the National Funding Authorities from Eight Involved Countries under Grant 826417. *(Corresponding author: Junzhong Xu.)*

Yang Wu, Pavol Bauer, and Zian Qin are with the Department of Electrical Sustainable Energy, DCE&S Group, Delft University of Technology, 2628 CD Delft, The Netherlands (e-mail: y.wu-6@tudelft.nl; p.bauer@tudelft.nl; z.qin-2@tudelft.nl).

Junzhong Xu is with the Department of Electrical Engineering, Shanghai Jiao Tong University, Shanghai 200240, China (e-mail: junzhongxu@sjtu.edu.cn).

Thiago Batista Soeiro is with the Faculty of Electrical Engineering, Mathematics and Computer Science (EEMCS), University of Twente, 7522 NB Enschede, The Netherlands (e-mail: t.batistasoeiro@utwente.nl).

Digital Object Identifier 10.1109/TTE.2024.3381167

TABLE I

SUMMARY OF THE SWITCHING FREQUENCY PROFILES FROM THE STUDIED LITERATURE [7], [8], [9], [10], [11], [12], [13], [14], [15], [16], [17], [18], [19], [20], [21], [22], [23], [24], [25], [26]

Reference	Circuit Type	Switching Frequency Profile						3-Φ* adoption	Purpose of use
		f_c (kHz)	$\Delta f_c/f_{c0}$*	f_m/f_o	$\theta_{k=1}$ (°)	Periodic	Sinusoid		
[7]	3-Φ AC	1.6–12	0.765	2	270	Yes	Yes	No	Switching Loss Optimization
[8]	3-Φ AC	5–15	0.5	2	90	Yes	No	No	
[9]	1-Φ AC	16.7–90	0.687	2	0	Yes	No	No	
[10]	1-Φ AC	2.5–10	0.6	2	270	Yes	No	No	
[11]	3-Φ AC	100–174	0.27	3	90	Yes	No	Yes	Zero-Voltage-Switching (ZVS)
[12]	3-Φ AC	100–146	0.187	3	90	Yes	No	Yes	
[13]	3-Φ AC	48–140	0.49	2	270	Yes	Yes	No	
[14]	1-Φ AC	35–75	0.36	2	90	Yes	No	No	
[15]	1-Φ AC	8–24	0.5	6	90	Yes	No	No	Current Ripple Reduction
[16]	3-Φ AC	6–10	0.25	6	270	Yes	No	Yes	
[17]	3-Φ AC	6–10	0.25	6	90	Yes	Yes	Yes	Voltage Ripple Reduction
[18]	3-Φ AC	6–10	0.25	6	270	Yes	No	Yes	
[19]	DC	75–105	0.167	-	-	Yes	Yes	-	Electromagnetic-Interference (EMI) Improvement
[20]	DC	30–166	0.69	-	-	Yes	No	-	
[21]	DC	108–132	0.1	-	-	Yes	Yes	-	
[22]	DC	140–260	0.3	-	-	Yes	No	-	
[23]	DC	52–148	0.48	-	-	Yes	Yes	-	
[24]	DC	140–260	0.3	-	-	Yes	No	-	
[25]	1-Φ AC	9–11	0.1	2	0	Yes	No	No	
[26]	3-Φ AC	25–50	0.333	6	270	Yes	No	Yes	

* Δf_c refers to the peak deviation of the switching frequency with regard to the centered frequency f_{c0}.
* 3-Φ adoption refers that the three phases of the converter implement the exactly the same frequency profile. 'No' can typically mean that the three phases adopt the switching frequency profile with same shape but different phase shift.

the different carrier-frequency harmonics bands, as presented in Fig. 2. It can be found that the most published VSFPWM methods unfortunately result in the overlap between the first- and second-harmonic band spectra, which might lead to an increased harmonic peak, as depicted in Fig. 3. As a result, more filtering efforts are required to comply with the harmonic emission standards in the concerned frequency range. In [19], [20], [21], [22], [23], and [24], the frequency profile can be designed with restricted frequency variation to avoid the spectra overlap to some extent while trading off the performance of EMI reduction. Besides harmonic spectra overlap, there is also lack of harmonic spectral analysis for power electronics converters implementing the variable-switching frequency at present. The spectra model of a single sinsuoidal harmonic modulated by the sinsuoidal frequency profile has been given and verified by [31] more than a decade ago. Prior to that, [23] has already analytically derived the output harmonics spectra under the sinusoidal switching frequency profile based on the PWM in a dc/dc converter. However, the derived model is simple in description but difficult for practical use due to the use of the impulse function (Dirac delta function). In [25], the output harmonic spectra under P-VSFPWM in a single-phase full-bridge converter were investigated, and the spectra model has been derived with the description of triple Fourier series. Unfortunately, the derived model is only applicable to the sinusoidal switching frequency profile. Hence, it is unable to deal with the harmonics generated by the rapidly emerged P-VSFPWM applications, since the most frequency profiles are nonsinusoidal as indicated by Table I. In [32], the harmonic spectra model under arbitrary P-VSFPWM profiles has been derived based on the triple Fourier summation form for the conventional three-phase two-level converter. However, the proposed algorithm to calculate the harmonic spectra is time-costly and not straightforward for practice, since it involves significant times of partition and iterations.

In this article, the P-VSFPWM-based interleaved converter is proposed to cancel out the odd-order carrier-frequency harmonic bands, as illustrated in Fig. 3, thus effectively mitigating the harmonic spectra overlap. Second, a generic harmonic spectra model under arbitrary periodic variable-switching frequency has been analytically derived, and an algorithm based on vectorization has been proposed for fast acquisition of the harmonic spectra. Moreover, the optimization of P-VSFPWM profile for minimal filter inductance based on the spectra model is also elaborated in detail. Finally, the proposed harmonic spectra model, spectral analysis, and the optimization are verified by the simulation and experiment on an interleaved two-level VSC converter, as shown in Fig. 4. The contributions of this article are as follows.

1) A fast-acquisition harmonic spectra model based on vectorizaion has been for the first time proposed for the grid-connected PWM converters implementing P-VSFPWM.
2) A comprehensive spectra analysis has been conducted to address the spectra symmetry of harmonics in one phase and between three phases under P-VSFPWM.
3) Twofold optimization of the P-VSFPWM profile: to minimize the size of filter without increasing supraharmonic peak or to significantly reduce supraharmonics while maintaining the same filter size.

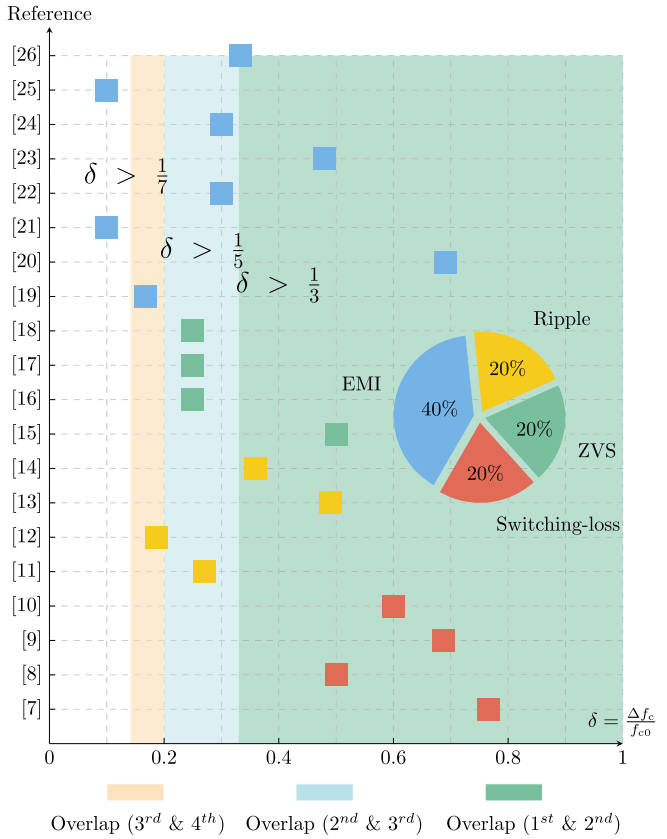

Fig. 2. Frequency variation coefficient $\delta = \Delta f_c / f_{c0}$ of the studied literature [7], [8], [9], [10], [11], [12], [13], [14], [15], [16], [17], [18], [19], [20], [21], [22], [23], [24], [25], [26]: the overlap of the sideband harmonics of the different carrier-frequency harmonics can be indicated by δ value based on Carson's rule [23].

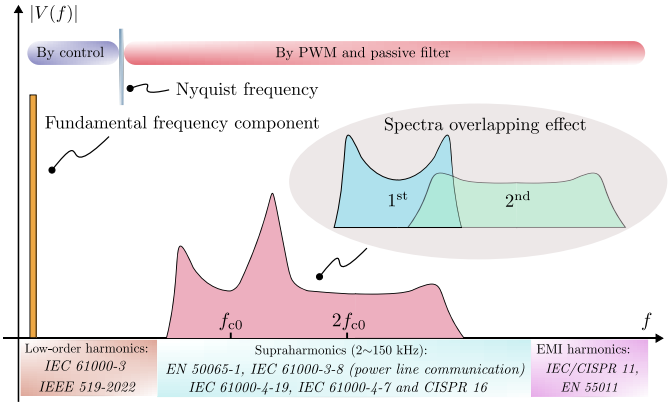

Fig. 3. Spectra overlap in the supraharmonics range due to VSFPWM operations.

The rest of this article is organized as follows. In Section II, the modeling of the two-interleaved PWM converter under the generic P-VSFPWM is presented. Section III introduces the fast-acquisition harmonic spectra model based on vectorization. A harmonic spectra analysis is elaborated in Section IV. In Section V, the design guidelines of the optimal P-VSFPWM profile are described. Section VI discusses the simulation and experimental results verifying the proposed harmonic spectra model and design. Finally, Section VI concludes this article.

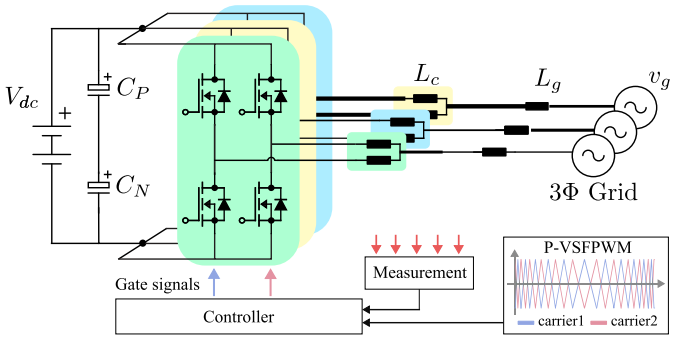

Fig. 4. Three-phase interleaved two-level VSC implementing P-VSFPWM.

II. Modeling of Interleaved Two-Level Converter Under P-VSFPWM

A. Harmonic Spectrum Model for CSFPWM

According to the double Fourier analysis (DFA) [33], the output voltage $V_c(x, y)$ of one bridge leg from the PWM converter depicted in Fig. 4 is the function of two independent variables

$$v_c(t) = \Re\left(\sum_{m=0}^{\infty}\sum_{n=-\infty}^{\infty} C_{mn} \cdot e^{j(mx+ny)}\right). \tag{1}$$

The two variables x and y represent the phases of the carrier and reference signals under the constant carrier-frequency modulation, respectively, which are expressed as follows:

$$\begin{cases} x(t) = \omega_c t + \theta_c \\ y(t) = \omega_o t + \theta_o \end{cases} \tag{2}$$

where ω_c and ω_o are the angular frequencies for the carrier and reference signals (switching and fundamental frequencies), respectively, and θ_c and θ_o are the phases for the carrier and reference signals. In (1), m and n are the multiples of the carrier and reference signal frequencies, while C_{mn} is the magnitude of the complex-form coefficients derived by using the double Fourier integral (DFI)

$$A_{mn} + jB_{mn} = \frac{1}{2\pi^2}\int_{-\pi}^{\pi}\int_{-\pi}^{\pi} v_c(x, y)e^{j(mx+ny)}\mathrm{d}x\mathrm{d}y$$
$$C_{mn} = \sqrt{{A_{mn}}^2 + {B_{mn}}^2}. \tag{3}$$

It is noteworthy that C_{mn} is determined by the implemented modulation method, e.g., the type of the carrier signal (saw-tooth or triangle) and the regular sampling (symmetrical or asymmetrical). Under the carrier-based PWM strategy of the interleaved converter, the two interleaved bridge legs share the same modulation reference signal but adopt the opposite triangle carriers, which are interleaved by 180°, as depicted in Fig. 5. Hence, one has

$$\begin{cases} x_1 = x_2 + \pi \\ y_1 = y_2 \end{cases} \tag{4}$$

where x_1 and x_2 are the phases of the two carrier signals, respectively. Taking one phase of the interleaved converter as an example, the two interleaved bridge legs can be represented by the circuitry shown in Fig. 6, where v_{c1} and v_{c2} are

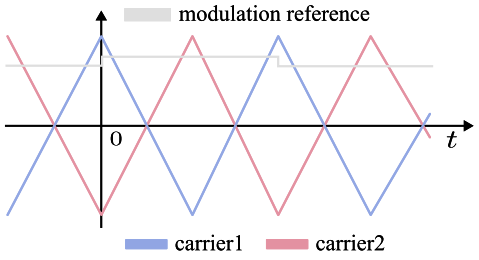

Fig. 5. Carrier-based PWM for the interleaved two-level PWM converter.

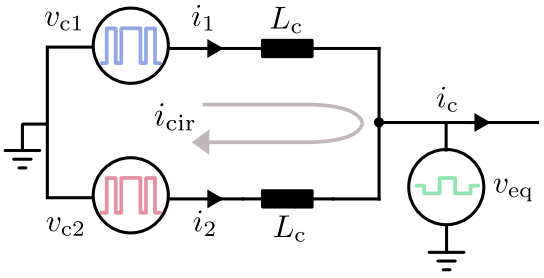

Fig. 6. Circuit simplification of the interleaved bridge legs.

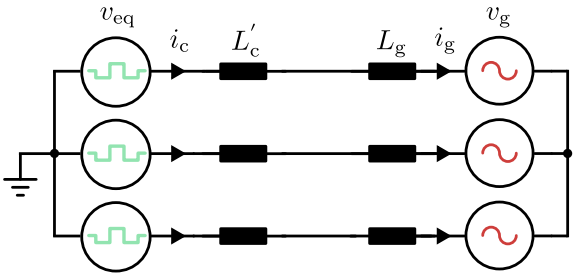

Fig. 7. Equivalent three-phase circuit representation of the grid-tied interleaved two-level converter with CIs.

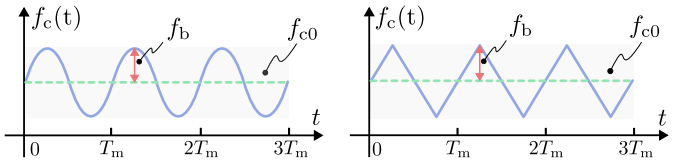

Fig. 8. Commonly used periodic switching frequency profiles. (a) Sinusoidal profile. (b) Triangular profile.

the output voltages of the interleaved bridge legs. v_{eq} is the equivalent output voltage to the load, which is the concern of the supraharmonic sources. Based on the Kirchhoff's laws through circuit analysis, one can obtain the followings:

$$\begin{cases} v_{c1} - v_{eq} = L_c \dfrac{di_1}{dt} \\ v_{c2} - v_{eq} = L_c \dfrac{di_2}{dt} \\ i_1 = i_c/2 + i_{cir} \\ i_2 = i_c/2 - i_{cir} \end{cases} \tag{5}$$

where i_{cir} is the circulating current and L_c is the converter-side inductance for each bridge leg. Furthermore, (5) can be simplified as follows:

$$v_{eq} = \frac{v_{c1} + v_{c2}}{2} - \frac{L_c}{2} \cdot \frac{di_c}{dt} = \frac{v_{c1} + v_{c2}}{2} - L_c' \frac{di_c}{dt}. \tag{6}$$

Based on (6), the equivalent three-phase circuit of the grid-tied two-level interleaved converter with the hard-paralleling inductors is described in Fig. 7, where the effective inductance contributing to the filtering of the switching harmonics is reduced to half.

From the harmonics point of view, the equivalent voltage v_{eq} now becomes

$$v_{eq} = \frac{v_{c1} + v_{c2}}{2} \tag{7}$$

and is the only supraharmonic sources from the PWM converter to the grid. Combining (1), (4), and (7), the time-domain expression of v_{eq} is obtained as follows:

$$v_{eq}(t) = \Re\left(\underbrace{\sum_{m=0}^{\infty} \sum_{n=-\infty}^{\infty} C_{mn} \cdot e^{j(mx+ny)}}_{m=0,2,4,6,8,\ldots} \right). \tag{8}$$

It can be noted that v_{eq} still remains the same expression in time domain, while its odd-times carrier-frequency harmonics vanish due to the interleaving method. Only the even-times carrier-frequency harmonics exist with the same magnitude as that in the noninterleaved PWM converter.

B. Harmonic Spectrum Model for P-VSFPWM

When the periodic VSFPWM is applied, the phases of the carrier and modulation reference signals are modified as follows:

$$\begin{cases} x(t) = 2\pi \displaystyle\int_0^t f_c(\tau) d\tau + \theta_c \\ y(t) = \omega_o t + \theta_o \end{cases} \tag{9}$$

where the periodic frequency $f_c(t)$ can be generally expressed with the following Fourier series:

$$f_c(t) = f_{c0} + \sum_{k=1}^{\infty} C_k \sin(2\pi k f_m t + \theta_k) \tag{10}$$

where f_{c0} is the centered switching frequency and f_m is the frequency of the periodic switching profile. Some typical periodic profiles, such as sinusoidal and triangular profiles, are illustrated in Fig. 8, where f_b is the peak deviation of the frequency from the centered frequency. Typically, $f_b = C_1$ for the sinusoidal profile.

The harmonic spectrum model of the converter output voltage under P-VSFPWM, hence, becomes extremely complicated, since the new variable $f_c(t)$ is coupled with $x(t)$, and thus, the triple Fourier analysis (TFA) is not applicable. By substituting (9) and (10) into (1), the time-domain expression of the bridge-leg output voltage under P-VSFPWM is derived as follows:

$$v_c(t) = \Re\left(\sum_{m=0}^{\infty} \sum_{n=-\infty}^{\infty} C_{mn} \cdot e^{j(2\pi(m \int_0^t f_c(\tau) d\tau + n f_o t) + \theta_{mn})} \right)$$

$$= \Re\left(\sum_{m=0}^{\infty}\sum_{n=-\infty}^{\infty}\left\{C_{mn}\cdot e^{j(2\pi(mf_{c0}+nf_o)t+\theta_{mn}+\varphi_m)}\right.\right.$$
$$\left.\left.\cdot \underbrace{\prod_{k=1}^{\infty} e^{-j\frac{mC_k}{kf_m}\cos(2\pi kf_m t+\theta_k)}}_{\text{multiplication term due to P-VSFPWM}}\right\}\right) \tag{11}$$

where

$$\theta_{mn} = m\theta_c + n\theta_o$$
$$\varphi_m = \sum_{k=1}^{\infty}\frac{mC_k\cos(\theta_k)}{kf_m}. \tag{12}$$

In (11), the multiplication term is contributed by the varying switching frequency. It can be noted that the model is not straightforward in the perspective of harmonic magnitude and indirect to be used for calculation. In [32], therefore, the model has been simplified and derived into the triple-summation series form by implementing Jacobi–Anger expansions [33]. Combined with the previously discussed merits of the interleaved bridge legs, v_{eq} under the P-VSFPWM can be formulated as follows:

$$v_{\text{eq}}(t) = \Re\left(\sum_{m=0}^{\infty}\sum_{n=-\infty}^{\infty}\sum_{l=-\infty}^{\infty}\underbrace{\left\{C_{mnl}\cdot e^{j2\pi(mf_{c0}t+nf_o t+lf_m t)}\right\}}_{m=0,2,4,6,8,\ldots}\right) \tag{13}$$

where

$$C_{mnl} = C_{mn}\cdot e^{j(\theta_{mn}+\varphi_m)}\cdot h(m,l) \tag{14}$$
$$h(m,l) = \sum_{\sum r_k\cdot k=l}\left(\prod_{k=1}^{\infty}J_r\left(\frac{mC_k}{kf_m}\right)\cdot e^{j(r(\theta_k-\pi/2))}\right) \tag{15}$$

where $J_n(x)$ is the Bessel function of the first kind. In (14), C_{mn} can be expressed as follows:

$$C_{mn} = \frac{2V_{\text{dc}}J_n\left[\left(m+n\frac{\omega_o}{\omega_{c0}}\right)\frac{\pi M}{2}\right]}{\pi\left(m+n\frac{\omega_o}{\omega_{c0}}\right)}\sin\left[\left(m+n\frac{\omega_o}{\omega_{c0}}+n\right)\frac{\pi}{2}\right]. \tag{16}$$

when the symmetrical sampling is applied with the sinusoidal pulsewidth-modulation (SPWM) strategy. Specifically, when $f_c(t)$ is a sinusoid with the frequency f_m, the coefficient C_{mnl} is reduced to

$$C_{mnl} = C_{mn}J_l\left(\frac{mC_1}{f_m}\right)\cdot e^{j(\theta_{mn}+\varphi_m+l(\theta_1-\pi/2))} \tag{17}$$

which is simpler to be calculated. It should be highlighted that the triple-summation series form in (13) is also applicable to other PWM methods, such as THIPWM (third-harmonic-injection PWM), SVPWM (space-vector PWM), and DPWM (discontinuous PWM) [33]. However, in this work, only SPWM is adopted for the sake of simplicity in analysis.

III. Proposed Fast-Acquisition Harmonic Spectra Model Based on Vectorization

A. Vectorization-Based Algorithm

It is noteworthy that (13) describes only the individual harmonic content with magnitude and phase at the frequency determined by m, n, and l. However, the harmonic at a certain frequency is the sum of these individual harmonics, which share the same frequency due to the different combinations of m, n, and l. Hence, the harmonic spectra of the output voltage in the interleaved two-level converter cannot be directly calculated based on (13). In [32], a calculation algorithm based on partition has been proposed to generate the voltage spectra. However, this algorithm requires significant amount of partition operations and iterations and, hence, becomes very complicated for practical use. Instead, a spectra-acquisition algorithm based on the vectorization operation is proposed in this work for faster calculation of the harmonics spectra

$$\boldsymbol{N} = \underbrace{\begin{bmatrix} N & \cdots & N \\ \vdots & \ddots & \vdots \\ -N & \cdots & -N \end{bmatrix}}_{2h\cdot L+1}\Bigg\}2N+1$$
$$\boldsymbol{C_{mn}} = \underbrace{\begin{bmatrix} C_{m,N} & \cdots & C_{m,N} \\ \vdots & \ddots & \vdots \\ C_{m,-N} & \cdots & C_{m,-N} \end{bmatrix}}_{2h\cdot L+1}\Bigg\}2N+1$$
$$\Theta_{\mathbf{mn}} = \underbrace{\begin{bmatrix} \theta_{m,N}+\varphi_m & \cdots & \theta_{m,N}+\varphi_m \\ \vdots & \ddots & \vdots \\ \theta_{m,-N}+\varphi_m & \cdots & \theta_{m,-N}+\varphi_m \end{bmatrix}}_{2h\cdot L+1}\Bigg\}2N+1. \tag{18}$$

1) Step 1—Matrices Generation: To start with simply, matrices with the dimension $(2N+1)\times(2h\cdot L+1)$ presented in (18) and (19), where h is the ratio between f_m and f_o, are first constructed to define harmonics information, e.g., magnitude, phase, and spectral position of the mth carrier-frequency harmonics. For the convenience of harmonics, h is usually selected to be an integer as observed from Table I. It should be noted that the element in matrices $\boldsymbol{L_h}$ and $\boldsymbol{H_{ml}}$ only occurs every h columns, and the rest columns have the elements of 0. Hereafter, the matrix $\boldsymbol{C_{mnl}}$ can be established from the Hadamard product ($\odot$, also called elementwise product) and sum of these created matrices

$$\boldsymbol{C_{mnl}} = \boldsymbol{C_{mn}}\odot e^{j\Theta_{\mathbf{mn}}}\odot\boldsymbol{H_{ml}}$$
$$\boldsymbol{R_{mnl}} = m\cdot M_f + \boldsymbol{N} + \boldsymbol{L_h} \tag{20}$$

where M_f is the ratio between f_{c0} and f_o.

2) Step2—Vector Acquisition: The matrices $\boldsymbol{C_{mnl}}$ and $\boldsymbol{R_{mnl}}$ contain the spectral information of the harmonics in terms of magnitude and frequency position. Each diagonal of $\boldsymbol{R_{mnl}}$ indicates a certain frequency, where the corresponding diagonal of $\boldsymbol{C_{mnl}}$ contains the individual harmonics. To obtain the resultant harmonic vector $\boldsymbol{H_m}$, the elements of the matrices should be summed up according to the diagonals

$$\boldsymbol{H_m} = \text{diag}(\boldsymbol{C_{mnl}}) \tag{21}$$

where the function diag sums up each diagonal of an arbitrary matrix into a vector and can be easily found and implemented on various programming platforms, such as MATLAB and Python.

Different from $\boldsymbol{H}_{\mathbf{m}}$, the harmonic position vector $\boldsymbol{P}_{\mathbf{m}}$ is formed by the following:

$$\begin{aligned}\boldsymbol{P}_{\mathbf{m}} &= \text{trace}(\boldsymbol{R}_{\mathbf{mnl}}) \\ &= m \cdot M_f + \left[-N - h \cdot L \quad \cdots \quad 0 \quad \cdots \quad N + h \cdot L\right]\end{aligned} \tag{22}$$

where the function trace is to acquire the outermost element of the matrix from bottom left to top right. This can be done by concatenating either the first column and row or the last row and column with the direction from bottom left to top right. The harmonic vectors $\boldsymbol{H}_{\mathbf{m}}$ represent the mth carrier-frequency switching harmonics with their spectral positions (harmonic order) listed in vector $\boldsymbol{P}_{\mathbf{m}}$. The size of the two vectors is $1 \times (2N + 2h \cdot L + 1)$, indicating that the harmonic sideband ranges from $-(N + h \cdot L)$ to $(N + h \cdot L)$ for the mth carrier-frequency switching harmonics.

However, the accuracy of $\boldsymbol{H}_{\mathbf{m}}$ decreases with the increase in m if the same N and L are used to calculate the carrier-frequency harmonics for all orders. This is because the harmonics range of $\boldsymbol{H}_{\mathbf{m}}$ naturally expands with multiplication of m, and the fixed size of $\boldsymbol{H}_{\mathbf{m}}$ might not include the entire harmonic spectrum scope. The same N and L with large enough values can be applied to all matrices regardless of m to avoid this inaccuracy. Nonetheless, the more computational efforts have to be traded off. Therefore, N_m and L_m are used instead of N and L for matrix generation

$$\begin{cases} N_m = m \cdot N_0 \\ L_m = m \cdot L_0 \end{cases} \tag{23}$$

where N_0 and L_0 are the fixed values independent of m. For instance, by applying (23), the matrix dimension for the second carrier-frequency harmonics will be doubled in both the length and width compared with that of the first carrier-frequency harmonics.

3) Step 3—Harmonic Spectra Concatenation: Thereafter, the harmonics generated in different carrier-frequency ranges (e.g., first, second, and third carrier-frequency harmonics) can be easily calculated. To attain the final harmonic spectra, the harmonic vectors $\boldsymbol{H}_{\mathbf{m}}$ with different m values should be concatenated into a new harmonic vector $\boldsymbol{H}$ with the range defined by the combined position vector $\boldsymbol{P}$

$$\begin{aligned}\boldsymbol{H} &= \text{cat}(\boldsymbol{H}_{\mathbf{m}}), \quad (m = 1, 2, 3, \ldots, m_{\max}) \\ \boldsymbol{P} &= \text{cat}(\boldsymbol{P}_{\mathbf{m}}), \quad (m = 1, 2, 3, \ldots, m_{\max}).\end{aligned} \tag{24}$$

The cat() function is realized by summing up the elements from all $\boldsymbol{H}_{\mathbf{m}}$ vectors (similar to $\boldsymbol{P}_{\mathbf{m}}$) at the same harmonic orders, as depicted in Fig. 9. The complete diagram of the proposed algorithm of the harmonic spectra acquisition under P-VSFPWM is demonstrated in Fig. 9. Besides, to obtain the voltage harmonic spectra with (13), some simplifications are adopted to accelerate the calculation with adequate accuracy. Usually, the first three terms in the Fourier series expansion of the periodic waveform can give a satisfactory approximation [32].

B. Differential-Mode (DM) Harmonics

In the three-phase three-wire ac/dc system, as illustrated in Fig. 3, only the DM currents can flow into the three-phase grid or load when considering supraharmonics frequency ranges. This is due to the inherent large impedance that prevents the common-mode (CM) or zero-sequence currents from flowing into the grid or load. From the interest of harmonics and supraharmonics emission and the related filter design, only the DM harmonic components are concerned in terms of the grid-side current harmonics. In general, the DM and CM components satisfy the following relations:

$$\begin{cases} x_a + x_b + x_c = 0, & \text{Differential-mode} \\ x_a = x_b = x_c, & \text{Common-mode} \\ v_{j,\text{dm}} = v_j - \dfrac{v_a + v_b + v_c}{3}, & (j = a, b, c) \end{cases} \tag{25}$$

where j represents the three-phase voltages and currents in the circuit. Alternatively, the terms with n equal zero, and the triple multiples in (13) should be rid of from the original harmonics in order to obtain only the DM harmonics components according to (13) and (24). However, this approach can be only used when the three phases adopt the same frequency profile.

Fig. 10 depicts the original and DM components of the converter output voltage under both CSFPWM and P-VSFPWM (sinusoidal profile). It can be seen that DM and CM components are separately lying in the spectrum. Moreover, the DM harmonic spectrum is only part of the original one and has lower magnitudes. Besides, it is noteworthy that the CSFPWM method only generates several considerable harmonics at $n = 0, \pm 2$, and ± 4. This feature can be used in the proposed algorithm to reduce the calculation time by setting $N \leqslant 4$.

$$\boldsymbol{L}_{\mathbf{h}} = \underbrace{\begin{bmatrix} -L \cdot h & \cdots & (-L+1) \cdot h & \cdots & (L-1) \cdot h & \cdots & L \cdot h \\ \vdots & \ddots & \vdots & \vdots & \vdots & \vdots & \vdots \\ -L \cdot h & \cdots & (-L+1) \cdot h & \cdots & (L-1) \cdot h & \cdots & L \cdot h \end{bmatrix}}_{2h \cdot L + 1} \Big\}_{2N+1}$$

$$\boldsymbol{H}_{\mathbf{ml}} = \underbrace{\begin{bmatrix} h(m, -L \cdot h) & \cdots & h(m, (-L+1) \cdot h) & \cdots & h(m, (L-1) \cdot h) & \cdots & h(m, L \cdot h) \\ \vdots & \ddots & \vdots & \vdots & \vdots & \vdots & \vdots \\ h(m, -L \cdot h) & \cdots & h(m, (-L+1) \cdot h) & \cdots & h(m, (L-1) \cdot h) & \cdots & h(m, L \cdot h) \end{bmatrix}}_{2h \cdot L + 1} \Big\}_{2N+1} \tag{19}$$

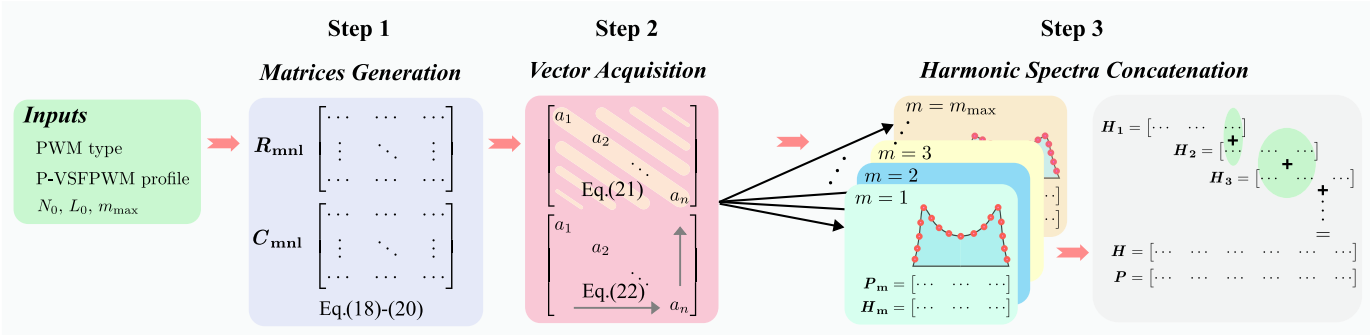

Fig. 9. Proposed harmonic spectra-acquisition algorithm based on vectorization.

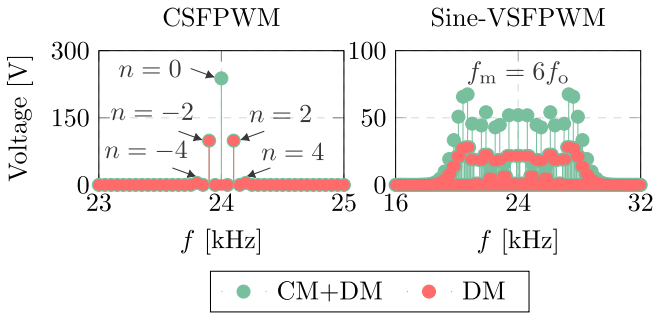

Fig. 10. Original (CM + DM) and DM components of the converter output voltage harmonics under CSFPWM and P-VSFPWM.

IV. Spectral Analysis of P-VSFPWM

A. Spectra Symmetry Between Three Phases

According to (11)–(15), each carrier-frequency harmonic spectrum of the converter output voltage is influenced by not only the frequency profile but also the modulation and carrier signals. In other words, the phase angle θ_{mn} and φ_m determine the shape of the spectrum significantly. Usually, θ_k is restricted by the intended P-VSFPWM application and, hence, cannot be modified. The influence of θ_c can be neglected by aligning the carrier and modulation signals. However, θ_o is inherently 120° phase-shifted between three phases, and the frequency profile for each phase has to be phase-shifted as follows to have the symmetrical output:

$$f_{cx}(t) = f_{c0} + \sum_{k=1}^{\infty} C_k \sin(2\pi k f_m t + k \cdot \theta_{ox} + \theta_k) \qquad (26)$$

where $x = a$–c. Compared with (10), where the three phases adopt the same frequency profile, (26) allows the three phases to operate P-VSFPWM independently. The spectra of the first carrier-frequency harmonics of the three-phase output voltages are presented in Fig. 11, with the frequency profiles determined by both (10) and (26) under $f_m = 2f_o$.

It can be noted that the three-phase output voltages are not symmetrical in terms of both original (CM + DM) and DM harmonics with the same frequency profile [obtained through (10)] applied to the three phases. By contrast, the three phases exhibit the same original (CM + DM) harmonics if three phase-shifted frequency profiles [obtained through (26)] are used for three phases, respectively.

Unfortunately, the DM components are still three-phase asymmetrical. In order to maintain three-phase symmetrical for both original (CM + DM) and DM harmonics, as shown in Fig. 11, f_m should be selected to be triple multiple of f_o [32]. In this case, (10) and (26) become the same, and the three phases adopt only one frequency profile. However, in other cases where f_m is not triple of f_o, the phase that has the largest critical harmonic [32] should be considered for the filter design.

B. Impact of f_m and θ_k on the Harmonic Spectrum

The phase shift θ_k plays a significant role in the spectrum shape of the P-VSFPWM output voltages. More specifically, the value of θ_1 determines the alignment difference between the frequency profile and the modulation reference signals [34]. It can be found in Table I that θ_1 is usually 0°, 90°, and 270° in the previous P-VSFPWM applications. Hence, the voltage spectrum (phase A) of the interleaved two-level converter is plotted in Fig. 12 under $\theta_1 = 0°$, 90°, 180°, and 270° to highlight the differences. It is worth mentioning that (10) is adopted for the switching frequency profiles of the three phases. Based on the results, it can be summarized as follows.

1) The value of θ_1 influences the shape of the voltage harmonics spectrum.
2) Both CM + DM and DM harmonic spectrum of $\theta_1 = 0°$ is symmetrical to that of $\theta_1 = 90°$ with regard to the axis $f = 2f_{c0}$. The same symmetry happens between the spectra of $\theta_1 = 90°$ and $\theta_1 = 270°$.
3) The harmonic spectrum has a larger peak when f_m equals even multiples ($2k$) of f_o as compared with odd multiples ($2k$–1).

Specifically, for the case $f_m = 6f_o$ depicted in Fig. 12, the DM voltage harmonic spectrum generated at $\theta_1 = 90°$ has its peak on the right-hand side of the axis $f = 2f_{c0}$. Consequently, it will lead to smaller current harmonic peaks compared with other cases of θ_1 values under the same filter, since the filter attenuates the voltage more with the increase in frequency. Therefore, this shape is preferred from the perspective of minimum filtering inductance for the harmonics emission standard.

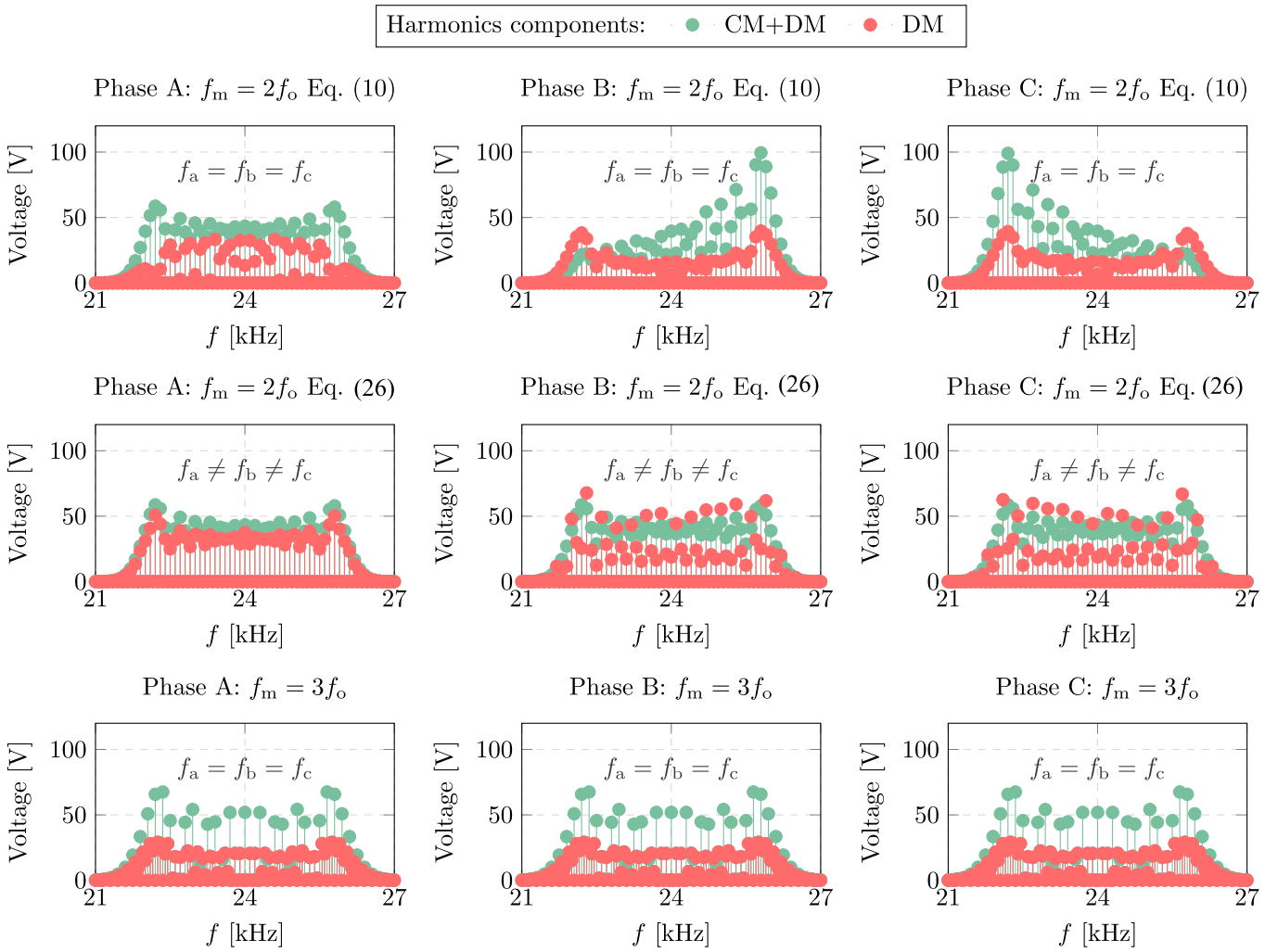

Fig. 11. Spectra of the three-phase output voltages with the sinusoidal frequency profiles determined by (10) and (26): $f_{C0} = 24.05$ kHz and $f_b = 2$ kHz.

C. Impact of Different EV Charging Power Conditions

In a PWM converter connected to a public grid, employing CSFPWM, e.g., SPWM, the switching harmonics are solely governed by the dc-link voltage [33], as indicated by (16). For both ac onboard and dc off-board fast-charging systems, the power electronics structure involves two stages: the grid-connected PFC converter and the isolated dc/dc converter, interconnected through the dc link. Charging typically adheres to a CC–CV (constant current–constant voltage) profile, resulting in variable charging power (load power) during operation. Nevertheless, the dc-link voltage remains constant during charging, regulated by the PFC rectifier's voltage controller. Consequently, switching harmonics remain consistent across different load power levels.

The PFC converter in the EV charging system is exclusively designed for operation at unit power factor (PF = 1), delivering pure active power to the load. Consequently, other power factor scenarios are not addressed in this article. Importantly, it should be noted that load conditions with varying power factors have no impact on the generated switching harmonics. This observation can be explained by (16), where differences in reactive power under distinct power factors only result in a phase angle shift of the modulation voltage reference, denoted by the shift in θ_o. This shift alters the phase of the switching harmonics as a whole but does not affect the magnitude of the switching harmonics C_{mn}.

Hence, various load conditions exert no influence on the switching harmonics generated through CSFPWM. Consequently, the impact of different load conditions on the switching harmonics generated by P-VSFPWM is identical. This uniform effect arises from the harmonics model of P-VSFPWM, which is established upon and derived from the CSFPWM model, as indicated by (13) and (14).

V. Optimized P-VSFPWM Design

In this section, an optimized P-VSFPWM design is devised aiming to not only satisfy the grid harmonic standards with less filtering, but also to keep the good performance of current harmonic distortion level and power efficiency close to which would be attained with the utilization of CSFPWM. As discussed earlier, f is selected to be triple multiple of f_o for the symmetrical three-phase harmonic spectra. Besides, f_m can also be chosen to be even multiple of f_o to locate all the switching harmonics only at odd-harmonic order [32],

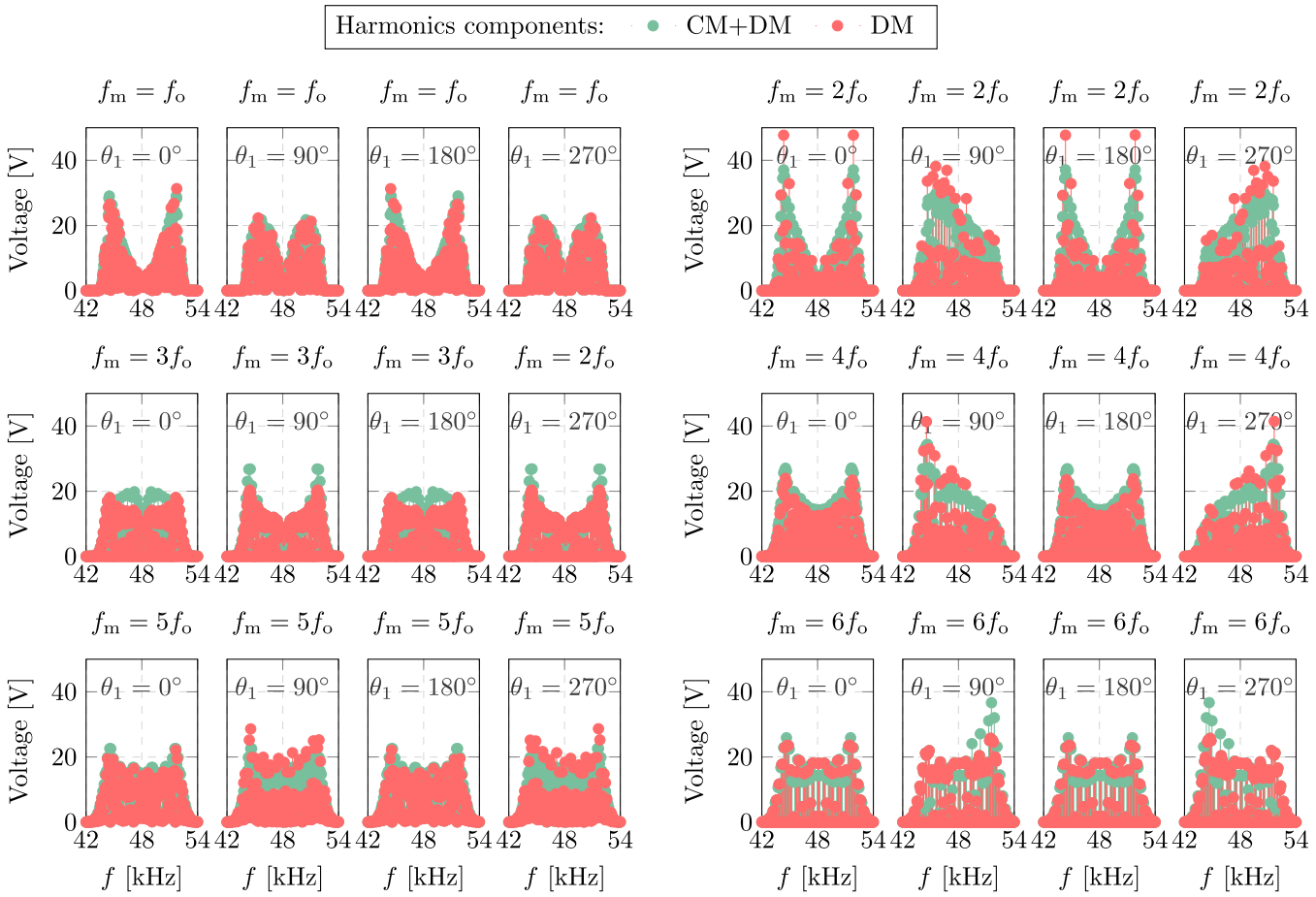

Fig. 12. Harmonic spectrum of (phase A) output voltage of the interleaved two-level converter under different values of f_m and θ_1 with sinusoidal profiles determined by (10): $f_{C0} = 24.05$ kHz and $f_b = 6$ kHz.

in order to avoid the stricter harmonics emission limit, e.g., IEEE 519-2022 [35] for the even-order harmonics. Therefore, $f_m = 6f_o$ is used in this work. Besides, θ_1 is selected to be 90°, as it requires less filtering and, hence, smaller inductance as compared with other values, according to Fig. 12 and the analysis in Section IV-B.

A. Filter Reduction by P-VSFPWM Optimization

The critical harmonic is defined as the most prominent peak harmonic in the current harmonic spectra [36], [37], [38]. This critical harmonic can be found by

$$I_{\text{crit}} = \|i(\omega_{\text{crit}})\| = \max\left\{\frac{\|v(\omega)\|}{\omega\left(L_c' + L_g\right)}\right\} \tag{27}$$

where ω starts from $\omega_{\min}$ to infinity. The minimum total required inductance to attenuate the critical harmonic below the emission limit I_{std} set by the supraharmonics standard is

$$L_{\text{T-req}} = \frac{V_{\text{crit}}}{\omega_{\text{crit}} I_{\text{std}}}. \tag{28}$$

Regarding the standards for supraharmonics, IEC 61000-4-30 has given an informative guidance in Annex C about this frequency range [29]. Useful information about measurement in supraharmonic range can be found in IEC 61000-4-7Annex B (2–9 kHz) and in CISPR 16 (9–150 kHz). Unfortunately, the standard for this frequency range is still evolving, and the supraharmonics emission limits are still under discussion. The suggested harmonic emission limit from the currently available standards, such as EN 50065-1 and IEC 61000-3-8, is only used for power line communication. Besides, the IEC 61000-4-19 standard is used for immunity test for the electrical and electronic equipment against conducted DM disturbances and signaling in the supraharmonics range but is not especially for the harmonic emission from the power electronic converter [30]. Hence, this work still uses the harmonic emission limits from IEEE 519 for simplicity of demonstration, because the main goal of the proposed P-VSFPWM is to show the relative reduction of require inductance under the same standard. The adoption of different standards does not affect this value.

In a symmetrical (between left and right of the spectrum) carrier-frequency harmonic spectrum of the converter output voltage, the critical harmonic is the one with the highest magnitude on the left-hand side, as depicted in Fig. 13, because the filtering attenuation increases with the frequency. However, the spectrum shape might not be symmetrical due to the various frequency profiles (as discussed in Section III). In some extreme cases where the peak voltage harmonic occurs on the right-hand side of the spectrum due to the frequency

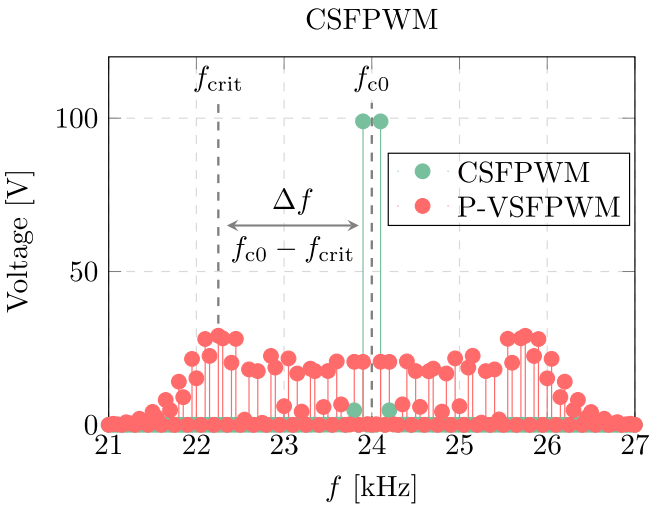

Fig. 13. Critical harmonic under the P-VSFPWM method.

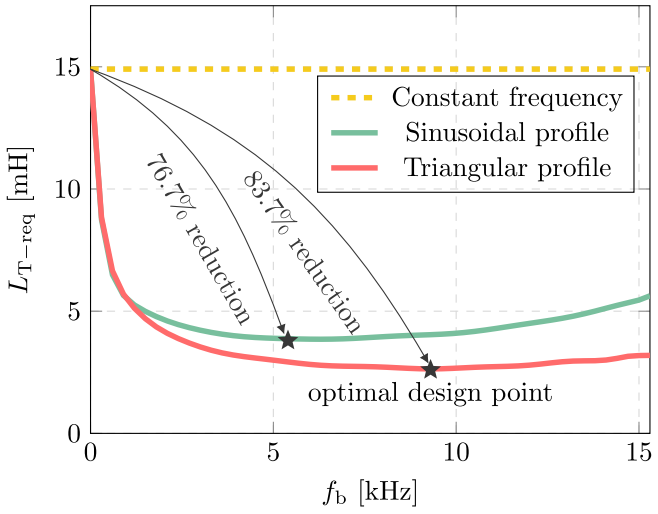

Fig. 14. Relation between L_T and f_b under the SPWM method with various frequency profiles for interleaved two-level VSC: $f_{c0} = 24.05$ kHz, $f_m = 6f_o$, and $\theta_1 = 90°$.

profile or the harmonics overlap, the critical harmonic is also located on the right-hand side of the centered frequency f_{c0}. In fact, such a harmonic spectra shape is preferred, since it lowers down the filtering demand compared with other cases. As demonstrated in Fig. 13, the distance between f_{c0} and f_{crit} is defined as Δf. Since the voltage harmonic spectra are symmetrical (both between phases and left-right sides) when $f_m = 6f_o$, the position of the critical harmonic is only associated with the frequency variation band f_b. It is interesting to observe this quantified relation in order to find a minimum critical harmonic under a certain filter or, in other words, the minimum required inductance $L_{\text{T-req}}$ (e.g., L filter) for the concerned harmonic standard. The relation between $L_{\text{T-req}}$ and f_b is depicted in Fig. 14 under the SPWM method with various frequency profiles for interleaved two-level converter, by using the parameters as listed in Table II. It is noteworthy that the required inductance under the periodic switching profiles always begins with a drop and then starts to increase at a certain value of f_b. Therefore, there is a clear minimum $L_{\text{T-req}}$ point for the P-VSFPWM profiles when f_b changes. Both sinusoidal and triangular profiles lead to the reduction of the required inductance compared with the constant frequency profile. More specifically, the triangle profile has a flatter function relation but results in a smaller required inductance value for L filter compared with sine profile. The maximum reduction for triangular and sinusoidal profiles is 83.7% and 76.7%, which are achieved at $f_b = 9300$ Hz and $f_b = 5400$ Hz, respectively. Although Fig. 14 presents only the case of $\theta_1 = 90°$, the value of θ_1 has negligible impact on this relation depicted in Fig. 14 based on the analysis in Section IV-B.

B. Trade-Off: Carrier-Frequency Harmonic Distortion (CHD)

As the trade-off to reshaping the harmonic peak by the P-VSFPWM methods, harmonics, which are concentrated at several frequencies, are spread over a wide range of frequency. Based on Carson's rule [23], the energy brought by these harmonics will remain after the frequency changed from CSFPWM to P-VSFPWM. Roughly, 98% of the energy is spread over the harmonics residing in the frequency band B_h, as depicted in Fig. 15, which can be roughly estimated by

$$B_n = 2(f_m + n \cdot f_b) \tag{29}$$

where h is the carrier-frequency harmonic order. In other words, the following relations are satisfied:

$$\begin{aligned} \text{CHD}_{v,n} &= \sum_{h \in B_n} V_{h\text{-VSF}}^2 \approxeq \sum V_{h\text{-CSF}}^2 \\ \text{CHD}_v &= \sqrt{\sum_n \text{CHD}_{v,n}^2} \end{aligned} \tag{30}$$

where $\text{CHD}_{v,n}$ measures the voltage CHD level of certain carrier-frequency harmonic band B_n, and CHD_v measures the CHD level over the whole frequency range. Under the filter with inductance L, CHD of the current can be similarly derived as follows:

$$\begin{aligned} \text{CHD}_{i,n} &= \frac{1}{I_1} \cdot \sqrt{\sum_{h \in B_n} \left(\frac{V_{h\text{-VSF}}}{\omega_h L} \right)^2} \\ \text{CHD}_i &= \sqrt{\sum_n \text{CHD}_{i,n}^2} \end{aligned} \tag{31}$$

where I_1 is the fundamental current component of the converter under the rated power and h is the harmonic order inside the carrier-frequency band B_n. It is important to highlight that CHD essentially reflects the distortion level of the waveform, as it encapsulates the root-mean-square (rms) information of the waveform. Assuming a symmetrical DM voltage harmonic spectrum of the nth carrier-frequency harmonics, by combining (29)–(31) together, it can it can be proved that the CHD_{i-n} of the P-SVFPWM is always larger than that of CSFPWM.

In fact, this has also been verified by Fig. 16, which sums up the CHD generated by various switching profiles under the SPWM method in the interleaved two-level VSC till

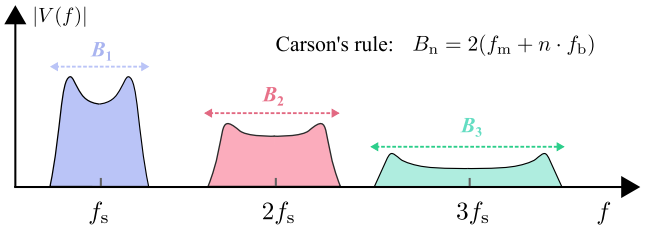

Fig. 15. Illustration of the frequency band accommodating 98% harmonics generated by the P-VSFPWM method.

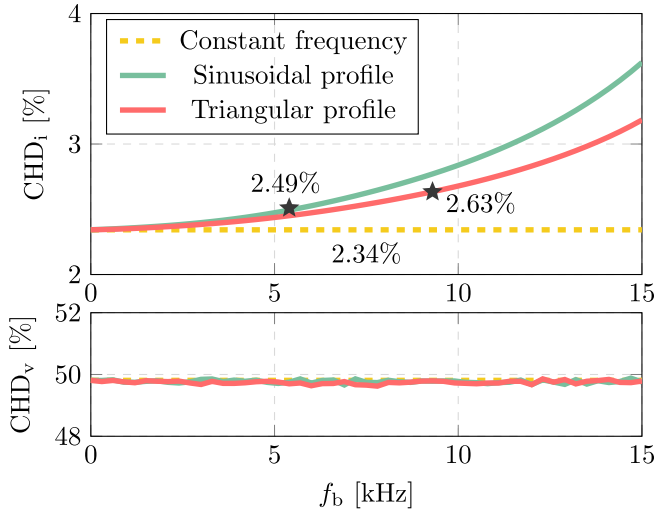

Fig. 16. Current and voltage CHD of the interleaved two-level VSC under the SPWM method with various frequency profiles: $f_{c0} = 24.05$ kHz, $f_m = 6f_o$, and $\theta_1 = 90°$.

150 kHz. Since the interleaved two-level VSC cancels out the odd carrier-frequency harmonics, only the second and fourth carrier-frequency harmonics are included in the calculation of CHD considering the supraharmonics range.

It is crucial to emphasize that various P-VSFPWM profiles, including CSFPWM, exhibit an identical level of harmonic distortion in the converter's output voltage, provided they share a centered switching frequency f_{c0}. This has been verified by Fig. 16, where the switching frequency (carrier-frequency) harmonics distortion CHD_v remains nearly constant irrespective of the periodic profiles and the frequency variation band f_b. Consequently, voltage harmonics are not a reliable indicator for assessing the harmonics performance of the P-VSFPWM profiles. It can be found in Fig. 16 that the CHD_i under P-VSFPWM is always larger than that of CSFPWM, which corresponds to the previous analysis. With the increase in f_b, CHD_i always increases, which clearly is the trade-off for the reduced current harmonic peak brought by P-VSFPWM. Therefore, the current instead of voltage harmonics is analyzed in this article to evaluate different P-VSFPWM profiles. According to Fig. 14, CHD_i is 2.63% and 2.49%, respectively, for the selected optimal profiles, which was only increased by 12.4% and 6.4% as compared with 2.34% CHD_i of CSFPWM.

C. Impact and Limitation of P-VSFPWM Optimization

In addition to addressing CHD, it is important to consider other trade-offs and potential negative impacts associated with this optimization process. These include the possibility of overlapped harmonic spectra and low-frequency resonance issues. Harmonic overlap becomes more likely when the frequency variation band f_b is sufficiently large. Low-frequency resonance can occur when the centered frequency f_{c0} is low, and f_b is large enough, potentially leading to interactions between the first carrier-frequency switching harmonic and the LC or LCL filter resonance. Fortunately, these side effects have been effectively mitigated through the adoption of an interleaved topology and the use of an L filter in this work.

The proposed optimization is only applicable to the PWM converter implementing P-VSFPWM or other spread-spectrum techniques. The PWM converters, e.g., two-level, multilevel, cascaded H-bridge (CHB), and modular multilevel converters, can be analyzed by the DFA approach, and the switching harmonic model for CSFPWM can be subsequently obtained in a similar way. The same mathematical manipulations from (11) to (13) can be used to derive the switching harmonics model in triple-summation form for these topologies implementing P-VSFPWM. The attenuation (or admittance) of the filter, e.g., L, LC, LCL, and even higher order types, changes opposite to V_{crit} as f_b varies, indicating the existence of the minimum $L_{\text{T-req}}$.

TABLE II
SYSTEM PARAMETERS FOR SIMULATION AND EXPERIMENT

PARAMETER	VALUE
Grid interface	
Voltage V_{ac} (rms)	230 V
Fundamental frequency f_o	50 Hz
Converter-side inductance L_{c}	340 μH
Grid-side inductance L_{g}	2.28 mH
Converter	
Semiconductor	IKW15N120BH6
Blocking voltage V_{B}	1200 V
Collector current I_{C}	15 A ($T_{\text{c}} = 100°$)
Operating power	3.3 kW
V_{dc}	700 V
C_{dc}	365 μF
f_{c0}	24.05 kHz
Modulation	
PWM	SPWM
Frequency profile	CSFPWM, Triangular Sinusoidal

D. Discussion on Harmonics Overlap

The harmonics overlap between different carrier-frequency harmonic bands usually results in an enhanced harmonic peak in the output voltage of the PWM converter. In normal cases, this enhanced harmonic peak is not concerned for quite some cases, because the critical harmonic still appears in the left half-part of the first carrier-frequency harmonic band after the overlap between the first and second carrier-frequency harmonic bands. However, in other scenarios, for instance, the spectrum under $f_m = 2f_o$ and $\theta_1 = 270°$ shown in Fig. 12,

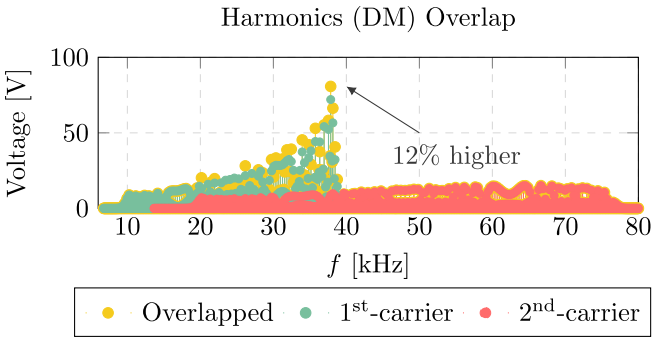

Fig. 17. Overlap from the first and second carrier-frequency harmonics.

the overlap between the different harmonic bands increases the critical harmonic by a considerable amount, as depicted in Fig. 17.

In fact, several approaches can be adopted to avoid or minimize this effect. First, f_m can be selected to be large enough, so that the spectrum shape becomes quasi-symmetrical, which is proved by Fig. 12. Hence, the critical harmonic is located in the left half-part of the spectra regardless of the overlap. Another alternative method is to adopt LCL filter instead of L filter. The critical voltage harmonic located at the right half-part will be shifted to the left-hand side by the much higher attenuation brought by the LCL filter. Hence, the harmonic increment caused by overlap is not critical for filter design. However, these approaches cannot be applied to applications where the profile and passive elements are already selected and fixed for specific purposes, such as ZVS operation. This work adopts the interleaved circuit structure, which can cancel out the odd-harmonic bands to avoid the harmonics overlap. Meanwhile, the profiles and operations used for the noninterleaved topology still apply to the interleaved circuit. In this interleaved operation, the switching profile used for the original operation should be halved, for instance, $f_{c0} = 48.05$ kHz and $f_b = 32$ kHz become $f_{c0} = 24.05$ kHz and $f_b = 16$ kHz, so that the semiconductor switching losses can be minimized for this interleaved operation. Hence, the only trade-off by this method is the circuitry complexity due to the doubled number of switches.

VI. Simulation and Experimental Verification

To verify the accuracy of the proposed algorithm and the optimal switching profiles for the minimum required inductance, both simulation and experimental tests are conducted in the three-phase interleaved two-level VSC depicted in Fig. 4. First, a PLECS-based simulation is carried out. Thereafter, the adopted periodic switching profiles are realized on a digitally controlled hardware platform, as shown in Fig. 18, with the DSP TMS320F28379D from Texas Instruments. The key specifications of the considered VSC are listed in Table II.

The conducted experiments uses a 10-kW rated prototype based on the three-phase interleaved converter illustrated in Fig. 18. The power semiconductors employed for this setup consist of 12 1200-V class discrete IGBTs (IKW15N120BH6) provided by Infineon Technologies, with antiparallel diodes. For thermal management, natural convection PCB-mounted

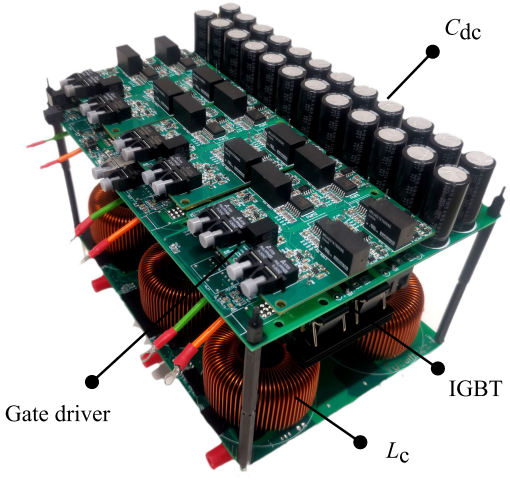

(a)

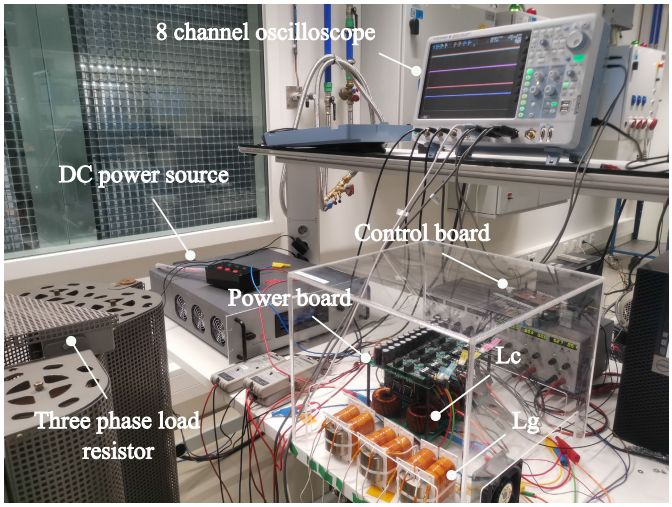

(b)

Fig. 18. Interleaved VSC prototype and experimental test bench. (a) Prototype. (b) Test bench.

heat sinks are employed to maintain safe device junction temperatures. The control system is facilitated by a 200-MHz dual-core microcontroller unit (MCU) from Texas Instruments, integrated into a LaunchPad development kit. A user-PC controls the programed operating modes within the MCU through a USB communication link. Importantly, this link is electrically isolated using an XDS100v2 debug probe for safety and precision. Furthermore, to ensure a high CM rejection ratio (CMRR) and prioritize safety, the control and power boards are interconnected via optical fiber links. In implementing the conventional d–q controller, all necessary analog-to-digital conversions (ADC) of inverter-related measurements—such as ac converter and grid-side terminal currents, ac grid voltages, and dc terminal voltages—are carried out on the power board using 10-MHz delta–sigma modulators. The acquired data are then transmitted to the MCU's sigma–delta filter channels via a 50-BMd fiber optic transmitter.

The inductor L_c depicted in Fig. 18(a) is built with two identical toroidal-core inductors with 340 μH, which are measured with an impedance analyzer. The grid-side inductor

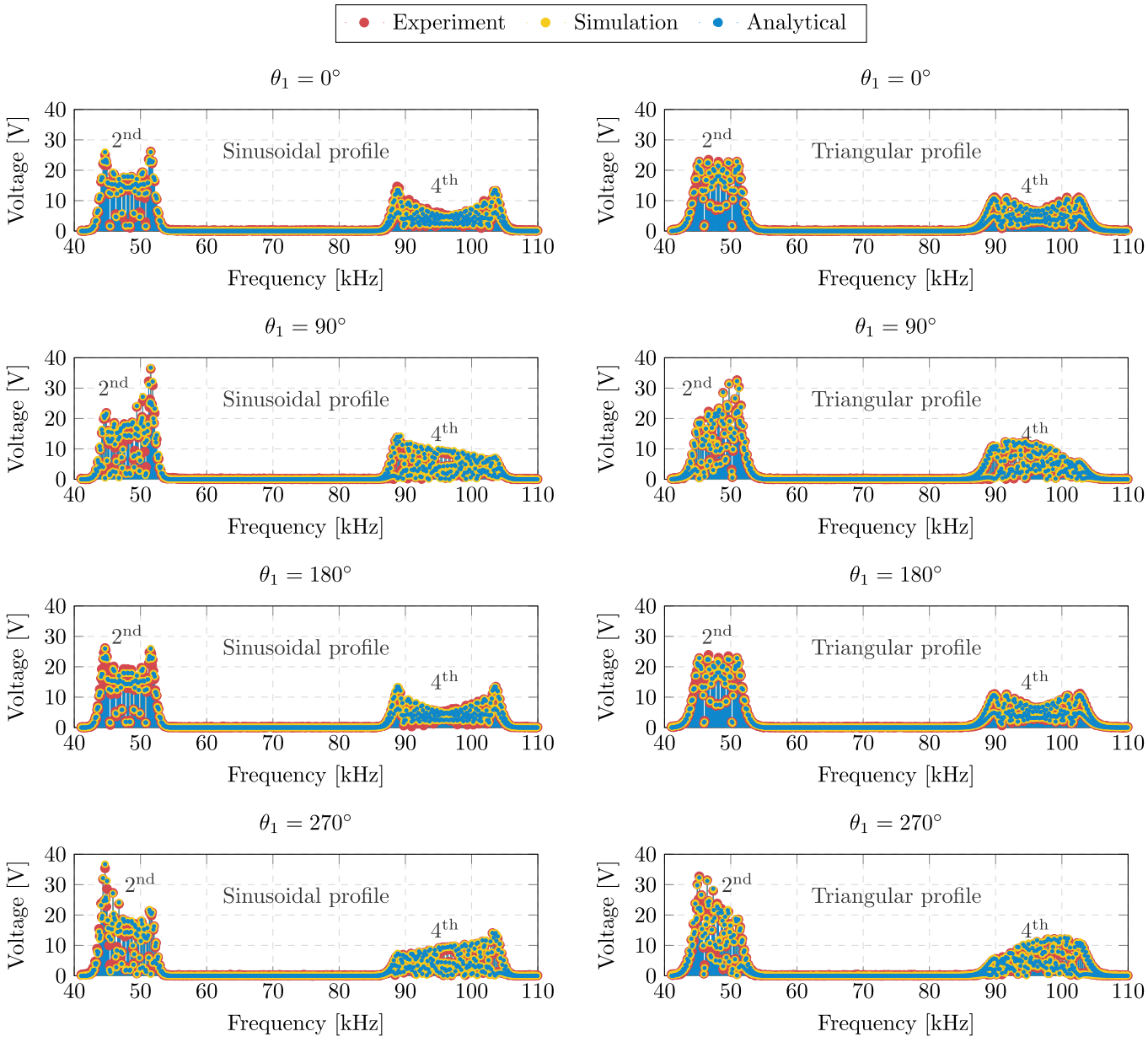

Fig. 19. Spectra comparison among analytical, simulation, and experimental results: the voltage harmonic spectra (phase A) of the interleaved two-level converter under $f_{C0} = 24.05$ kHz, $f_b = 2$ kHz, and $f_m = 6f_o$. Both the sinusoidal and triangular periodic profiles were tested at $\theta_1 = 0°$, 90°, 180°, and 270°.

L_g is built with amorphous cut-core (AMCC, also called Metglas) material and litz wire and rated as 2.28 mH. The component value selection was devised using the design guideline presented in Section V while considering the SPWM method and triangular profile. For experiment, the three-phase interleaved two-level VSC is operated in the inverter mode at full power factor. All of the experimental waveforms and data used in this article are recorded by the oscilloscope YOKOGAYA DLM5038.

A. Verification of the Proposed Harmonic Spectra Model

The voltage harmonic spectra (phase A) of the interleaved two-level converter under $f_{C0} = 24.05$ kHz, $f_b = 2$ kHz, and $f_m = 6f_o$ were obtained through conducting FFT analysis of the converter output voltage measured from the simulation and experiment. Both the sinusoidal and triangular periodic profiles were tested at $\theta_1 = 0°$, 90°, 180°, and 270°. The correctness of the proposed harmonic spectra-acquisition method is be validated by comparing the analytical harmonic spectra obtained based on Fig. 9 with those acquired from both the simulation and experimental results. Fig. 19 presents the harmonic spectra of the interleaved two-level VSC output voltage (phase a) from the analytical, simulation, and experimental results. Because of interleaving, the harmonic spectra are resided around 48.1 kHz (second carrier-frequency harmonics) and 96.2 kHz (fourth carrier-frequency harmonics). It can be found that the spectra shape of the second carrier-frequency harmonics is consistent with those presented in Fig. 12, which validates the impact of θ_k on the harmonic spectrum. It can be clearly noted that the

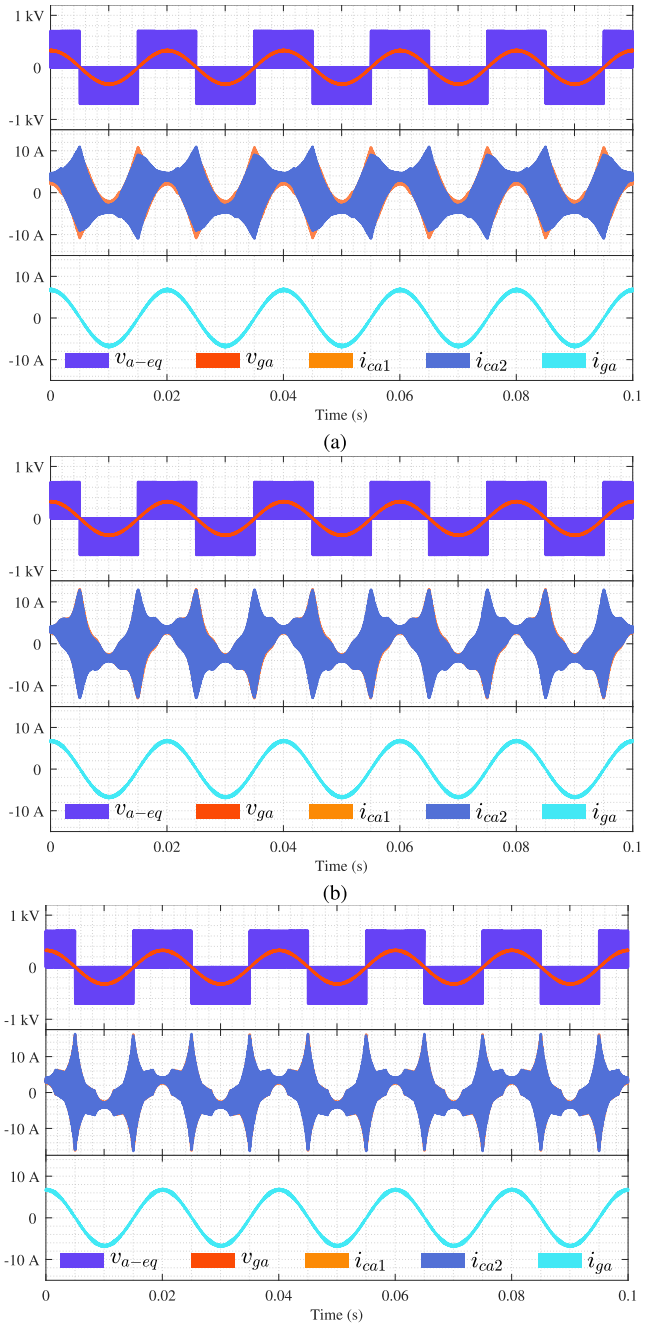

Fig. 20. Simulation waveforms of the three-phase interleaved two-level converter under the optimal profiles listed in Table III. (a) Waveforms under CSFPWM. (b) Waveforms under the optimal sinusoidal profile. (c) Waveforms under the optimal triangular profile.

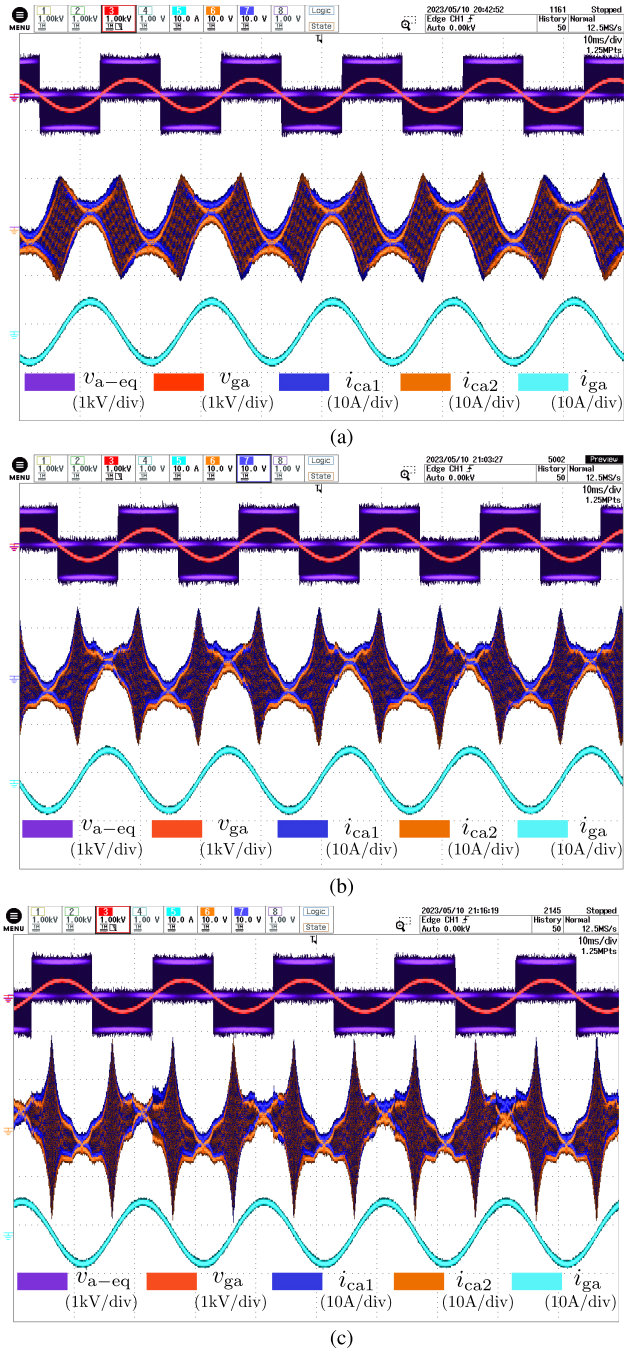

Fig. 21. Experimental waveforms of the three-phase interleaved two-level converter under the optimal profiles listed in Table III. (a) Waveforms under CSFPWM. (b) Waveforms under the optimal sinusoidal profile. (c) Waveforms under the optimal triangular profile.

analytical harmonic spectra based on the proposed algorithm accurately match the simulated voltage harmonic spectra in all cases. Even for the fourth carrier-frequency harmonics components, which cost much longer computational efforts with the algorithm proposed by [32], it can be easily calculated with a very high accuracy (maximum difference at critical harmonic: 0.2 V, 0.6%) to the simulation results. When compared with the experimental results, the analytical voltage harmonic spectra have a visible but negligible difference (maximum difference at critical harmonic: 1.35 V, 3.8%). The difference between the simulation and experimental results might be caused by the periodic switching frequency discretized by the DSP, whose f_m and f_b values can be slightly offset from the set values. Besides, the difference can also be resulted by the variation of the dc-link voltage by the dc power source. Finally, the unbalance between the three-phase load can lead to the asymmetry between the three-phase spectra.

B. Optimal Profiles for Minimum L_T

The optimal switching profiles leading to the minimum requirement of L_T are listed in Table III. The simulation and experimental waveforms under the optimal switching profiles

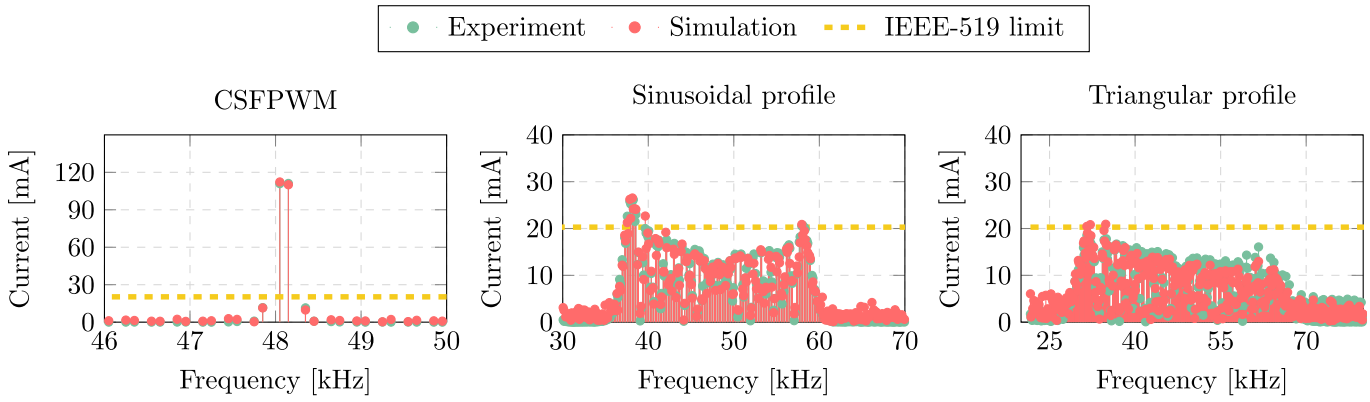

Fig. 22. Spectra comparison among analytical, simulation, and experimental results: the current harmonic spectra (phase A) of the interleaved two-level converter under $f_{C0} = 24.05$ kHz, $f_b = 2$ kHz, and $f_m = 6f_o$.

TABLE III
RECORDS FOR THE OPTIMAL PROFILES SHOWN IN FIG. 14

Switching Profile	I_{crit}* (%)		TRD* (%)		CHD (%)		η* (%)
	Simu*	Exp*	Simu	Exp	Simu	Exp	Exp
CSFPWM							
f_{c0}=24.05 kHz	1.642	1.756	0.121	0.522	2.478	2.863	97.12
Sinusoidal							
f_{b}=5400 Hz	0.387	0.392	0.092	0.523	2.543	2.913	97.09
Triangular							
f_{b}=9300 Hz	0.2844	0.309	0.1183	0.657	2.637	2.948	97.07

* I_{crit} refers to the ratio between the critical current harmonic and the rated load peak current.
* TRD is the total rated-current distortion and calculates the low-order harmonics till 2 kHz.
* Simu and Exp refer to the simulation and experiment results.
* η refers to the tested system efficiency.

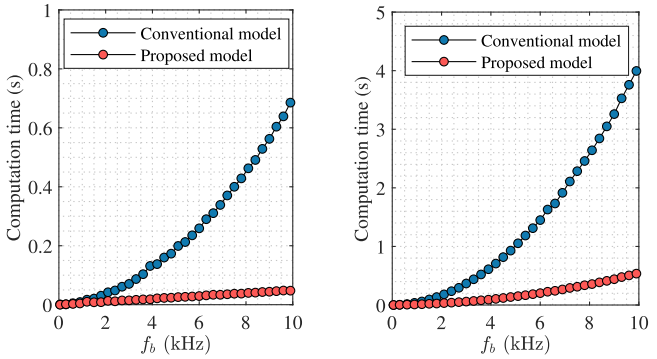

(a) Sinusoidal profile (b) Triangular profile

Fig. 23. Comparison of the computational time cost between the model in [32] and the proposed model. (a) Sinusoidal profile. (b) Triangular profile.

at 3.3-kW load power are presented in Figs. 20 and 21, respectively. The experimental results closely resemble the simulation waveforms across all profiles. Nevertheless, there is a slight variance between the experimental and simulation results for i_{ca1} and i_{ca2} when the load current reaches its peak. This discrepancy can be attributed to the inherent differences between the two inductors, L_c, in the interleaved bridges. In practice, these inductors are not perfectly identical due to manufacturing and materials variations.

Both simulated and experimental harmonic spectra of the grid-side current under the optimal profiles are depicted in Fig. 22 for a better comparison against the IEEE-519 emission limit. Table III records the critical harmonic with regard to the rated load peak current. Compared with other cases, the current harmonics generated by the triangular profile match the emission limit of 0.3% set by the IEEE-519. The I_{crit} for triangular profile is 5 times smaller than that of CSFPWM. In other words, a five times smaller inductor can be adopted to triangular profile to achieve the same critical current harmonic peak compared with CSFPWM. The total rated-current distortion (TRD) [39] is used in this article to evaluate the low-order harmonics distortion level, which calculates the total root sum square of the current distortion components in percentage of the converter rated current instead of load current. The measured TRD from experiment results are larger than the simulated ones in all cases. This difference could be resulted by the nonideal dc voltage source, asymmetry of the three-phase circuitry parameters and slightly unbalanced three-phase load. However, it can be noted that the TRD values for all three cases are close to each other, which indicates a negligible impact on the TRD from the P-VSFPWM methods.

Regarding the CHD analysis, it is worth noting that the experimental results show slightly higher values than the simulated ones. This discrepancy may arise from high-frequency noise that the oscilloscope recorded during the experiments. Similarly, the CHD values for sinusoidal and triangular profiles are marginally higher than those for CSFPWM, which is a trade-off for reducing harmonic peaks. Both simulation and experimental waveforms clearly indicate that periodic switching profiles result in higher current ripple in the converter output current (i_{ca1} and i_{ca2}) compared with CSFPWM. This ripple increases, as the frequency variation band f_b increases. In summary, it can be concluded that P-VSFPWM significantly reduces the required inductance at a minor expense in terms of CHD and current ripple.

The converter system efficiency under the three switching profiles remains almost unchanged, which are 97.12%, 97.09%, and 97.07%, respectively. This indicates that the selected periodic switching profiles will not lead to extra

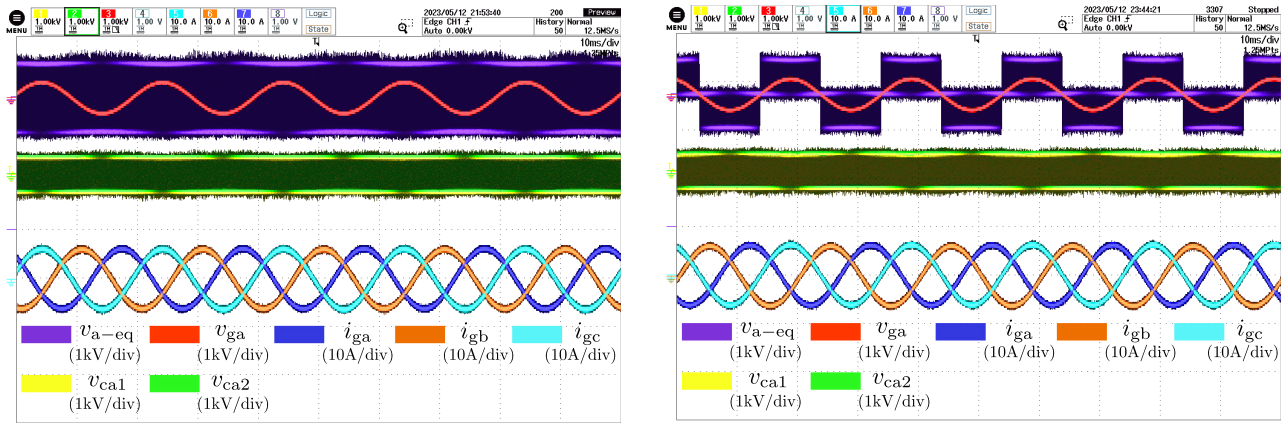

Fig. 24. Experimental waveforms with the sinusoidal switching profile under two different operations: (a) hard paralleling: $f_m = 2f_o$, $f_{C0} = 48.05$kHz, and $f_b = 16$ kHz and (b) interleaving: $f_m = 2f_o$, $f_{C0} = 24.05$kHz, and $f_b = 16$ kHz.

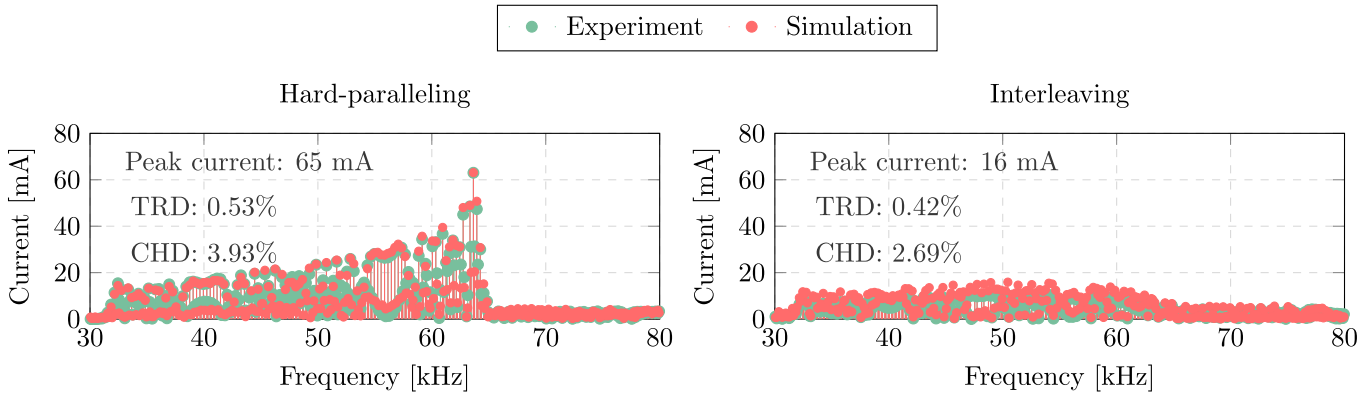

Fig. 25. Experimental and simulated grid current harmonic spectra under hard-paralleling and interleaved operations.

switching losses, which is also proven in [32]. However, the periodic switching profiles result in higher switching ripples, which can lead to higher semiconductor conduction loss and inductor loss, which can explain the slight decrease of the efficiency under the sinusoidal and triangular profiles.

C. Computational Time for the Proposed Model

The vectorization-based model proposed in this article offers a significant computational advantage over the conventional harmonic spectra model by eliminating numerous calculation loops. A comparison of computation time for generating the first carrier-frequency harmonic spectrum using both models [32] reveals that the proposed method reduces the calculation time by eight times for optimal sinusoidal and triangular profiles, as listed in Table IV. Specifically, computation time increases exponentially with f_b in sinusoidal and triangular profiles with the conventional method, while the proposed model shows a linear relationship for sinusoidal profiles, as shown in Fig. 23. Triangular profiles exhibit an exponential relationship with a smaller curvature compared with the conventional model. This demonstrates the superiority of the proposed approach.

D. Mitigation of Harmonics Overlap

In order to verify the effectiveness of the interleaving in mitigating the harmonics overlap due to the large variation of the frequency band f_b under some common P-VSFPWM operations, for instance, the ZVS operation conducted by [13] the sinusoidal profile has been tested under both hard-paralleling and interleaving operations. In this case, the sinusoidal switching profile with $f_m = 2f_o$ and $\theta_1 = 270°$ is adopted in order to realize ZVS operation for both positive and negative cycles of the fundamental period. Therefore, $f_m = 2f_o$, $f_{C0} = 48.05$ kHz, and $f_b = 16$ kHz and $f_m = 2f_o$, $f_{C0} = 24.05$ kHz, and $f_b = 8$ kHz are used for hard-paralleling and interleaving operations, respectively. The experimental waveforms are shown in Fig. 24 for both operations. By conducting FFT analysis on the harmonic spectra of the three-phase grid currents, the current spectra are obtained and depicted in Fig. 25 for a clear comparison.

First, the experimental current harmonic spectra match the simulated ones with a quite good accuracy. Besides, the current harmonic peak has been significantly reduced from 65 to 16 mA, which is roughly a 75% reduction. Meanwhile, both

TABLE IV
COMPUTATION TIME COMPARISON

Switching Profile	Computation time (s)	
	Proposed model	Model in [32]
Sinusoidal: f_b=5400 Hz	0.3028	0.252
Triangular: f_b=9300 Hz	0.479	3.630

TRD and CHD in interleaved operation have a considerable drop compared with hard-paralleling operation. It is also noteworthy that the semiconductor losses under two cases will be similar, since the switching frequency is halved for interleaved operation, and the converter remains to be the identical one.

It is also worthy to mention that the selected converter might not be the optimized design for the hard-paralleling operation in terms of ratings and semiconductor loss metrics. If the noninterleaving operation is directly applied to an optimized conventional three-phase two-level VSC based on six switches instead of using hard-paralleled topology, the harmonics performance will still remain the same, as shown in Fig. 25. However, the power losses of the two converters will depend on the selection of the power components.

E. Loss Analysis of P-VSFPWM Profile

The rms current, semiconductor loss, and inductor loss are obtained based on the time-based simulation results in MATLAB and presented in Fig. 26. The adoption of P-VSFPWM results in higher switching ripple, leading to increased rms currents. Fig. 26(a) demonstrates that P-VSFPWM profiles influence converter-side rms current similar to current CHD. The grid-side current i_g experiences a negligible change due to the large grid-side filter inductance L_g.

Conduction loss associated with rms current follows a similar increasing trend as f_b. In contrast, switching losses decrease with increasing f_b. The switching energies $E_{\text{on,off},rr}$ are interpolated from the IGBT datasheet and expressed as the second-order polynomial functions, whose coefficients are a, b, and c. Assuming an ideal current $i(t) = I\sin(\omega_o t + \varphi)$, the switching loss under the proposed P-VSFPWM profile can be modeled as follows:

$$P_{\text{sw}} = P_{\text{sw0}} + \frac{4V_{\text{dc}}}{2\pi V_b b I}\sum_{k=1}^{\infty}\frac{C_k \sin(6k\varphi - \theta_k)}{36k^2 - 1} \tag{32}$$

where P_{sw0} is the switching loss under CSFPWM and V_b is the reference voltage in the datasheet. It is noteworthy that P-VSFPWM results in an additional term in the switching loss, which can be negative with certain P-VSFPWM profile and power factor angle. The P-VSFPWM design selected in this article leads to a smaller switching loss as compared with CSFPWM as $\varphi = 0$ (PFC operation) and $\theta_k = 90°$, which corresponds to the simulated switching loss. The inductor model incorporates core loss using iGSE (improved Steinmetz equation) and winding loss considering skin effect and proximity effect [40]. Inductor losses increase with f_b similar to current CHD, reflecting the relationship among core loss, winding loss, and current harmonics. However, for the grid-side inductor L_g, loss increment is minimal, remaining virtually unchanged with increasing f_b. Grid-side current, with fewer harmonics, exhibits less influence (minimal increase in rms current) with f_b. Winding loss dominates in the grid-side inductor, primarily determined by winding resistance and the fundamental current component. This clarifies the reason why the measured efficiency of the converter under CSFPWM and P-VSFPWM profiles is quite close, as the decreased switching losses are balanced out due to the increased conduction losses and inductor losses.

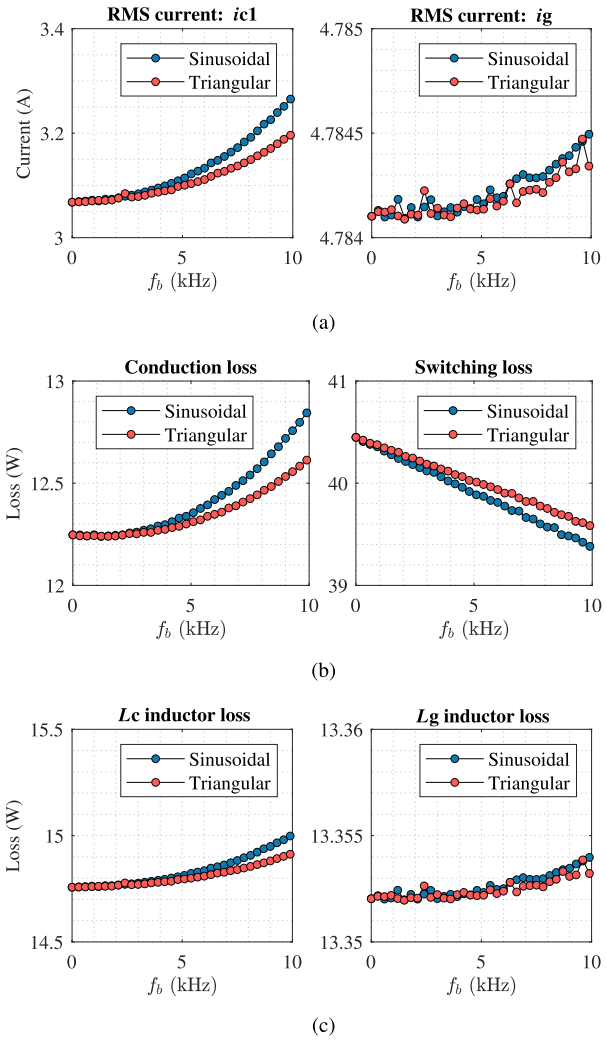

Fig. 26. Modeled losses under the P-VSFPWM profiles. (a) RMS currents. (b) Semiconductor device losses. (c) Inductor losses.

VII. Conclusion

This work proposes a generic fast-acquisition harmonic spectra model based on vectorization for the grid-connected PWM converter under P-VSFPWM. The P-VSFPWM method has been implemented in the three-phase, three-wire interleaved two-level ac/dc converter to mitigate the harmonic spectra overlap. A comprehensive harmonic spectral analysis is conducted to examine the influence of the periodic switching profile on the symmetry property of the harmonics. Through spectral analysis, optimal switching profiles are identified to achieve the minimum required inductance while complying with the current harmonic emission limit set by the IEEE-519 standard. The proposed generic harmonic spectra model and analysis are validated through both simulation and experimental results. The triangular profile is confirmed as the optimal choice, as it requires an inductance that is five times smaller than that of CSFPWM. Both simulation and experimental findings indicate an increase in the CHD, along with other analyzed trade-offs, during the implementation of P-VSFPWM. Furthermore, the effectiveness of interleaved operation in reducing harmonics overlap is demonstrated through experimental results, which also show improved har-

monic performance in terms of TRD and CHD. Overall, the proposed method provides valuable insights into the analysis and optimization of harmonic spectra in P-VSFPWM-based converters, supported by rigorous simulation and experimental validations.

REFERENCES

[1] Y. Li et al., "Optimal synergetic operation and experimental evaluation of an ultra-compact GaN-based three-phase 10 kW EV charger," *IEEE Trans. Transport. Electrific.*, early access, Jul. 28, 2023, doi: 10.1109/TTE.2023.3297502.

[2] D. Lyu, T. B. Soeiro, and P. Bauer, "Multi-objective design and benchmark of wide voltage range phase-shift full bridge DC/DC converters for EV charging application," *IEEE Trans. Transport. Electrific.*, vol. 10, no. 1, pp. 288–304, Mar. 2024, doi: 10.1109/TTE.2023.3254203.

[3] D. Lyu, T. B. Soeiro, and P. Bauer, "Design and implementation of a reconfigurable phase shift full-bridge converter for wide voltage range EV charging application," *IEEE Trans. Transport. Electrific.*, vol. 9, no. 1, pp. 1200–1214, Mar. 2023.

[4] W. Shi et al., "Design of a highly efficient 20-kW inductive power transfer system with improved misalignment performance," *IEEE Trans. Transport. Electrific.*, vol. 8, no. 2, pp. 2384–2399, Jun. 2022.

[5] D. Das, N. Weise, K. Basu, R. Baranwal, and N. Mohan, "A bidirectional soft-switched DAB-based single-stage three-phase AC–DC converter for V2G application," *IEEE Trans. Transport. Electrific.*, vol. 5, no. 1, pp. 186–199, Dec. 2019.

[6] J. Xu, T. B. Soeiro, Y. Wang, F. Gao, H. Tang, and P. Bauer, "A hybrid modulation featuring two-phase clamped discontinuous PWM and zero voltage switching for 99% efficient DC-type EV charger," *IEEE Trans. Veh. Technol.*, vol. 71, no. 2, pp. 1454–1465, Feb. 2022.

[7] R. Mandrioli, A. Viatkin, M. Hammami, M. Ricco, and G. Grandi, "Variable switching frequency PWM for three-phase four-wire split-capacitor inverter performance enhancement," *IEEE Trans. Power Electron.*, vol. 36, no. 12, pp. 13674–13685, Dec. 2021.

[8] O. Oñederra, I. Kortabarria, I. M. de Alegría, J. Andreu, and J. I. Gárate, "Three-phase VSI optimal switching loss reduction using variable switching frequency," *IEEE Trans. Power Electron.*, vol. 32, no. 8, pp. 6570–6576, Aug. 2017.

[9] X. Mao, R. Ayyanar, and H. K. Krishnamurthy, "Optimal variable switching frequency scheme for reducing switching loss in single-phase inverters based on time-domain ripple analysis," *IEEE Trans. Power Electron.*, vol. 24, no. 4, pp. 991–1001, Apr. 2009.

[10] H. A. Attia, T. K. S. Freddy, H. S. Che, W. P. Hew, and A. Elkhateb, "Confined band variable switching frequency pulse width modulation (CB-VSF PWM) for a single-phase inverter with an LCL filter," *IEEE Trans. Power Electron.*, vol. 32, no. 11, pp. 8593–8605, Nov. 2017.

[11] J. Chen, D. Sha, J. Zhang, and X. Liao, "A variable switching frequency space vector modulation technique for zero-voltage switching in two parallel interleaved three-phase inverters," *IEEE Trans. Power Electron.*, vol. 34, no. 7, pp. 6388–6398, Jul. 2019.

[12] J. Chen, D. Sha, J. Zhang, and X. Liao, "An SiC MOSFET based three-phase ZVS inverter employing variable switching frequency space vector PWM control," *IEEE Trans. Power Electron.*, vol. 34, no. 7, pp. 6320–6331, Jul. 2019.

[13] M. Haider et al., "Novel ZVS S-TCM modulation of three-phase AC/DC converters," *IEEE Open J. Power Electron.*, vol. 1, pp. 529–543, 2020.

[14] D. Rothmund, T. Guillod, D. Bortis, and J. W. Kolar, "99.1% efficient 10 kV SiC-based medium-voltage ZVS bidirectional single-phase PFC AC/DC stage," *IEEE J. Emerg. Sel. Topics Power Electron.*, vol. 7, no. 2, pp. 779–797, Jun. 2019.

[15] A. C. B. Kumar and G. Narayanan, "Variable-switching frequency PWM technique for induction motor drive to spread acoustic noise spectrum with reduced current ripple," *IEEE Trans. Ind. Appl.*, vol. 52, no. 5, pp. 3927–3938, Sep. 2016.

[16] Q. Li, D. Jiang, Z. Shen, Y. Zhang, and Z. Liu, "Variable switching frequency PWM strategy for high-frequency circulating current control in paralleled inverters with coupled inductors," *IEEE Trans. Power Electron.*, vol. 35, no. 5, pp. 5366–5380, May 2020.

[17] Q. Li and D. Jiang, "Variable switching frequency PWM strategy of two-level rectifier for DC-link voltage ripple control," *IEEE Trans. Power Electron.*, vol. 33, no. 8, pp. 7193–7202, Aug. 2018.

[18] Q. Li, X. Zhao, D. Jiang, and J. Chen, "Voltage ripple control of flying capacitor three-level inverter with variable switching frequency PSPWM," *IEEE Trans. Ind. Electron.*, vol. 69, no. 4, pp. 3313–3323, Apr. 2022.

[19] F. Lin and D. Y. Chen, "Reduction of power supply EMI emission by switching frequency modulation," *IEEE Trans. Power Electron.*, vol. 9, no. 1, pp. 132–137, Jan. 1994.

[20] M. Albach, "Conducted interference voltage of AC–DC converters," in *Proc. 17th Annu. IEEE Power Electron. Specialists Conf.*, Jun. 1986, pp. 203–212.

[21] A. Santolaria, J. Balcells, D. Gonzalez, and J. Gago, "Evaluation of switching frequency modulation in EMI emissions reduction applied to power converters," in *Proc. 29th Annu. Conf. IEEE Ind. Electron. Soc.*, vol. 3, Nov. 2003, pp. 2306–2311, doi: 10.1109/IECON.2003.1280604.

[22] D. Gonzalez et al., "Conducted EMI reduction in power converters by means of periodic switching frequency modulation," *IEEE Trans. Power Electron.*, vol. 22, no. 6, pp. 2271–2281, Nov. 2007.

[23] K. K. Tse, H. S.-H. Chung, S. Y. R. Hui, and H. C. So, "A comparative study of carrier-frequency modulation techniques for conducted EMI suppression in PWM converters," *IEEE Trans. Ind. Electron.*, vol. 49, no. 3, pp. 618–627, Jun. 2002.

[24] D. Gonzalez, J. T. Bialasiewicz, J. Balcells, and J. Gago, "Wavelet-based performance evaluation of power converters operating with modulated switching frequency," *IEEE Trans. Ind. Electron.*, vol. 55, no. 8, pp. 3167–3176, Aug. 2008.

[25] J. Huang and R. Xiong, "Study on modulating carrier frequency twice in SPWM single-phase inverter," *IEEE Trans. Power Electron.*, vol. 29, no. 7, pp. 3384–3392, Jul. 2014.

[26] J. Chen, D. Jiang, W. Sun, Z. Shen, and Y. Zhang, "A family of spread-spectrum modulation schemes based on distribution characteristics to reduce conducted EMI for power electronics converters," *IEEE Trans. Ind. Appl.*, vol. 56, no. 5, pp. 5142–5157, Sep. 2020.

[27] S. Schöttke, J. Meyer, P. Schegner, and S. Bachmann, "Emission in the frequency range of 2 kHz to 150 kHz caused by electrical vehicle charging," in *Proc. Int. Symp. Electromagn. Compat.*, Sep. 2014, pp. 620–625.

[28] C. Waniek, T. Wohlfahrt, J. M. A. Myrzik, J. Meyer, M. Klatt, and P. Schegner, "Supraharmonics: Root causes and interactions between multiple devices and the low voltage grid," in *Proc. IEEE PES Innov. Smart Grid Technol. Conf. Eur. (ISGT-Europe)*, Sep. 2017, pp. 1–6.

[29] L. Wang, Z. Qin, T. Slangen, P. Bauer, and T. van Wijk, "Grid impact of electric vehicle fast charging stations: Trends, standards, issues and mitigation measures—An overview," *IEEE Open J. Power Electron.*, vol. 2, pp. 56–74, 2021.

[30] M. Bollen, M. Olofsson, A. Larsson, S. Ronnberg, and M. Lundmark, "Standards for supraharmonics (2 to 150 kHz)," *IEEE Electromagn. Compat. Mag.*, vol. 3, no. 1, pp. 114–119, 1st Quart., 2014.

[31] J. Balcells, A. Santolaria, A. Orlandi, D. Gonzalez, and J. Gago, "EMI reduction in switched power converters using frequency modulation techniques," *IEEE Trans. Electromagn. Compat.*, vol. 47, no. 3, pp. 569–576, Aug. 2005.

[32] Y. Wu, J. Xu, T. B. Soeiro, M. Stecca, and P. Bauer, "Optimal periodic variable switching PWM for harmonic performance enhancement in grid-connected voltage source converters," *IEEE Trans. Power Electron.*, vol. 37, no. 6, pp. 7247–7262, Jun. 2022.

[33] D. G. Holmes and T. A. Lipo, *Pulse Width Modulation for Power Converters: Principles and Practice*. Piscataway, NJ, USA: IEEE Press, 2003.

[34] Y. Wu, Z. Qin, T. B. Soeiro, and P. Bauer, "Design guideline for PWM converter implementing periodic VSFPWM—A comprehensive analysis on the harmonics spectrum," in *Proc. 11th Int. Conf. Power Electron. ECCE Asia*, May 2023, pp. 1509–1516.

[35] *IEEE Standard for Harmonic Control in Electric Power Systems*, IEEE Standard 519-2022 (Revision IEEE Standard 519-2014), 2022, pp. 1–31.

[36] K. Jalili and S. Bernet, "Design of LCL filters of active-front-end two-level voltage-source converters," *IEEE Trans. Ind. Electron.*, vol. 56, no. 5, pp. 1674–1689, May 2009.

[37] K.-B. Park, P. Klaus, and R. M. Burkart, "Spread spectrum modulation for LCL filter design," in *Proc. 20th Int. Symp. Power Electron. (EE)*, Oct. 2019, pp. 1–6.

[38] Z. Quan, Y. W. Li, and C. Jiang, "Design of interleaved converters with minimum filtering requirement," in *Proc. IEEE Appl. Power Electron. Conf. Expo. (APEC)*, Mar. 2019, pp. 404–411.

[39] *IEEE Standard for Interconnection and Interoperability of Distributed Energy Resources With Associated Electric Power Systems Interfaces*, IEEE Standard 1547-2018, (Revision IEEE Standard 1547-2003), 2018, pp. 1–138.

[40] J. Muhlethaler, J. W. Kolar, and A. Ecklebe, "Loss modeling of inductive components employed in power electronic systems," in *Proc. 8th Int. Conf. Power Electron. (ECCE Asia)*, May 2011, pp. 945–952.

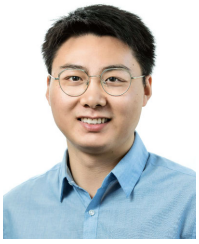

Yang Wu (Student Member, IEEE) received the B.S. degree in electrical engineering and automation from Southeast University, Nanjing, China, in 2017, and the M.Sc. degree (cum laude) in electrical power engineering from Delft University of Technology, Delft, The Netherlands, in 2019, where he is currently pursuing the Ph.D. degree in electrical engineering from DC Systems, Energy Conversion and Storage (DCES) Group.

From January to April 2024, he was a Visiting Scholar at Princeton Power Electronics Research Laboratory, Princeton University, Princeton, NJ, USA. His current research interests include the modeling, control, and variable switching frequency modulation of the power converter for grid applications.

Junzhong Xu (Member, IEEE) was born in Ningbo, China, in 1994. He received the B.S. degree in electrical engineering from Harbin Institute of Technology, Harbin, China, in 2016, and the Ph.D. degree in electrical engineering from Shanghai Jiao Tong University, Shanghai, China, in 2021.

From 2020 to 2021, he was a Visiting Scholar with the DC Systems, Energy Conversion and Storage Group, Delft University of Technology, Delft, The Netherlands. From 2021 to 2024, he worked as a Post-Doctoral Research Fellow with the Department of Electrical Engineering, Shanghai Jiao Tong University, and with the Power Electronic Systems (PES) Laboratory, Swiss Federal Institute of Technology (ETH), Zurich, Switzerland. His current research interests include advanced control and modulation for power converters.

Dr. Xu was a recipient of the Outstanding Ph.D. Thesis Award from Shanghai Jiao Tong University in 2021.

Thiago Batista Soeiro (Senior Member, IEEE) received the B.Sc. and M.Sc. degrees (Hons.) in electrical engineering from the Federal University of Santa Catarina, Florianopolis, Brazil, in 2004 and 2007, respectively, and the Ph.D. degree in electrical engineering from the Swiss Federal Institute of Technology, Zurich, Switzerland, in 2012.

During the master's and Ph.D. studies, he was a Visiting Scholar with the Power Electronics and Energy Research Group, Concordia University, Montreal, QC, Canada, and the Center for Power Electronics Systems, Blacksburg, VA, USA. From 2012 to 2013, he was a Researcher with the Power Electronics Institute, Federal University of Santa Catarina. From 2013 to 2018, he was with the Corporate Research Center, ABB Switzerland Ltd., Baden-Dattwil, Switzerland, where he was a Senior Scientist. From 2018 to 2022, he was with the DC Systems, Energy Conversion and Storage Group, Delft University of Technology, Delft, The Netherlands, where he was an Associate Professor. From January to October 2022, he was with the Power Management and Distribution Section for the European Space Research and Technology Center, Noordwijk, The Netherlands. Since October 2022, he has been a Full Professor of Power Electronics with the Power Electronics and Electromagnetic Compatibility Group, University of Twente, Enschede, The Netherlands. His current research interests include advanced high-power converters and dc system integration.

Pavol Bauer (Senior Member, IEEE) received the master's degree in electrical engineering from the Technical University of Kosice, Košice, Slovakia, in 1985, and the Ph.D. degree from Delft University of Technology, Delft, The Netherlands, in 1995.

He was a Title Professor at the President of Czech Republic, Brno University of Technology, Brno, Czechia, in 2008, and Delft University of Technology, in 2016. He is currently a Full Professor with the Department of Electrical Sustainable Energy, Delft University of Technology, and the Head of DC Systems, Energy Conversion and Storage Group. He has authored or coauthored over 72 journals and almost 300 conference papers (with H factor Google scholar 43 and Web of science 20), eight books, and holds four international patents, and he organized several tutorials at the international conferences. He has worked on many projects for industry concerning wind and wave energy, and power electronic applications for power systems, such as Smarttrafo; HVdc systems, projects for smart cities, such as PV charging of electric vehicles, PV and storage integration, and contactless charging, and he participated in several Leonardo da Vinci and H2020 EU projects as project partner (ELINA, INETELE, and E-Pragmatic) and coordinator (PEMCWebLab.com-Edipe, SustEner, and Eranet DCMICRO).

Zian Qin (Senior Member, IEEE) received the B.Eng. degree from Beihang University, Beijing, China, in 2009, the M.Eng. degree from Beijing Institute of Technology, Beijing, in 2012, and the Ph.D. degree from Aalborg University, Aalborg, Denmark, in 2015, all in electrical engineering.

In 2014, he was a Visiting Scientist at Aachen University, Aachen, Germany, and an Associate Professor at Delft University of Technology, Delft, The Netherlands. He has authored or coauthored more than 100 journals/conference papers, four book chapters, and two international patents, and also worked on several European and Dutch national projects in these areas. His current research interests include power quality and stability of power electronics-based grids and solid-state transformers.

Dr. Qin served as the Technical Program Chair of the IEEE-PEDG 2024, the IEEE-PEDG 2023, the IEEE-ISIE 2020, and the IEEE-COMPEL 2020. He is an Associate Editor of IEEE TRANSACTIONS ON INDUSTRIAL ELECTRONICS and a Guest Associate Editor of IEEE JOURNAL OF EMERGING AND SELECTED TOPICS and IEEE TRANSACTIONS ON ENERGY CONVERSION. He is a Distinguished Reviewer for 2020 of IEEE TRANSACTIONS ON INDUSTRIAL ELECTRONICS.